metals

MDPI

Review

Corrosion Resistance of Ultrathin Two-Dimensional Coatings: First-Principles Calculations towards In-Depth Mechanism Understanding and Precise Material Design

Tian-Yu Sun [1,2], Yu Hao [1,2], Ying-Hao Wu [1], Wen-Jie Zhao [1] and Liang-Feng Huang [1,*]

[1] Key Laboratory of Marine Materials and Related Technologies, Zhejiang Key Laboratory of Marine Materials and Protective Technologies, Ningbo Institute of Materials Technology and Engineering, Chinese Academy of Sciences, Ningbo 315201, China; suntianyu@nimte.ac.cn (T.-Y.S.); haoyu@nimte.ac.cn (Y.H.); wuyinghao@nimte.ac.cn (Y.-H.W.); zhaowj@nimte.ac.cn (W.-J.Z.)

[2] Center of Materials Science and Optoelectronics Engineering, University of Chinese Academy of Sciences, Beijing 100049, China

* Correspondence: huangliangfeng@nimte.ac.cn; Tel.: +86-0574-86683209

Abstract: In recent years, ultrathin two-dimensional (2D) coatings, e.g., graphene (Gr) and hexagonal boron nitride (h-BN), are intriguing research foci in the field of anticorrosion because their high air stability, excellent impermeability, high optical transparency, and atomistic thickness have endowed them with attractive anticorrosion applications. The microstructure of 2D coatings, coating–substrate interactions, and properties of 2D coatings on substrates in a variety of environmental conditions (e.g., at different temperatures, stresses, and pH values) are the key factors governing the anticorrosion performance of 2D coatings and are among the central topics for all 2D-coating studies. For many conventional experimental measurements (e.g., microscopy and electrochemical methods), there exist challenges to acquire detailed information on the atomistic mechanisms for the involved subnanometer scale corrosion problems. Alternatively, as a precise and efficient quantum-mechanical simulation approach, the first-principles calculation based on density-functional theory (DFT) has become a powerful way to study the thermodynamic and kinetic properties of materials on the atomic scale, as well as to clearly reveal the underlying microscopic mechanisms. In this review, we introduce the anticorrosion performance, existing problems, and optimization ways of Gr and h-BN coatings and summarize important recent DFT results on the critical and complex roles of coating defects and coating–substrate interfaces in governing their corrosion resistance. These DFT progresses have shed much light on the optimization ways towards better anticorrosion 2D coatings and also guided us to make a prospect on the further development directions and promising design schemes for superior anticorrosion ultrathin 2D coatings in the future.

Keywords: graphene; h-BN; metals; interfaces; defects; corrosion resistance

check for updates

Citation: Sun, T.-Y.; Hao, Y.; Wu, Y.-H.; Zhao, W.-J.; Huang, L.-F. Corrosion Resistance of Ultrathin Two-Dimensional Coatings: First-Principles Calculations towards In-Depth Mechanism Understanding and Precise Material Design. *Metals* **2021**, *11*, 2011. https://doi.org/10.3390/met11122011

Academic Editors: George A. Pantazopoulos and Frank Czerwinski

Received: 2 November 2021
Accepted: 10 December 2021
Published: 13 December 2021

Publisher's Note: MDPI stays neutral with regard to jurisdictional claims in published maps and institutional affiliations.

Copyright: © 2021 by the authors. Licensee MDPI, Basel, Switzerland. This article is an open access article distributed under the terms and conditions of the Creative Commons Attribution (CC BY) license (https://creativecommons.org/licenses/by/4.0/).

1. Introduction

Corrosion usually is an undesirable phenomenon since it negatively affects the performance of refined metal products related to infrastructures, water conservancy projects, transportation, energy, manufacturing, and public services and also leads to environmental pollution. The astonishing amount of corrosion costs (e.g., ~3.34% of the gross domestic product of China in 2014 [1]) clearly reflects the seriousness and magnitude of corrosion issues. Many protection methods have been developed to overcome the corrosion issues of structural alloys in the past few decades, and these corrosion protection methods can be divided into several categories, among which the major three ones are (1) *improving bulk-alloy corrosion resistance*, (2) *anticorrosion surface treatment*, and (3) *using protective coatings*. The third one (i.e., *using protective coatings*) is the most invested in anticorrosion approach due to its low cost, easy functionalization, and convenient and fast implementation [1].

Graphene (Gr) and hexagonal boron nitride (h-BN), as the two most prototypical two-dimensional (2D) materials, have been considered in the past decade to be ideal ultrathin coatings to protect metallic components working in various aggressive environments under the influence of many factors (e.g., stress, humidity, sunlight, temperature, wind, and biological activity) without changing the physical properties of the protected metallic substrate. This can be attributed to the fact that they simultaneously possess many superior intrinsic properties, e.g., subnanometer thickness, high chemical durability, impermeability to molecules and atoms, high transparency (97.7% for Gr), flexible and strong 2D lattice, high intrinsic strength (∼130 GPa for Gr and 120–165 GPa for h-BN) and Young's modulus (1000 GPa for Gr and 710–970 GPa for h-BN), and high electronic conductivity (10^8 m/s for Gr) or insulation (a ∼6 eV wide bandgap for h-BN) [2–7]. These outstanding intrinsic characteristics and excellent anticorrosion efficiencies have endued graphene and h-BN with a wide range of promising applications in aerospace planes, marine facilities, deep-sea drilling equipment, bathyscaphes, turbine engines/motors, precision mechanical and electronic equipment, and biomedical devices. In addition, the massive production of 2D materials having been realized in contemporary industry (e.g., over five thousands of tonnes of Gr produced worldwide in 2017 [8]) further positively contributes to the development and application potentials of 2D coatings.

Gr and h-BN, as genuine and prominent representatives of popular 2D coating materials in the field of anticorrosion and antioxidation, their basic properties and barrier properties in various environments have been extensively studied. Although there have been some nice review articles about the anticorrosion properties of Gr and h-BN coatings, the topics therein mainly focus on the experimental progresses in measurement and material synthesis, where theoretical studies are just sporadically mentioned [3,9–15]. The 2D-coating microstructures and environment–coating–substrate interactions in different conditions (e.g., marine environment, deep-sea high-pressure environment, cold polar environment, wetland environment, saline arid environment, etc.) are the key factors deciding the corrosion resistance of Gr and h-BN coatings. We have recently witnessed great experimental progress in the synthesis and characterization of anticorrosion 2D coatings, and many electrochemical testing methods (e.g., Tafel analysis, cyclic voltammetry, and electrochemical impedance spectroscopy) and characterization methods (e.g., X-ray diffraction, scanning electron microscopy, transmission electron microscopy, X-ray photoelectron spectroscopy, energy dispersive X-ray spectroscopy, scanning tunneling microscopy, and atomic force microscopy) have been jointly used to reveal many important corrosion behaviors and the relevant underlying mechanisms [3,9–15]. However, it is still challenging in the existing experiments to precisely understand the complex multiple-factor synergistic coupling mechanisms, i.e., the interactions between 2D-coating defects, coating–substrate interfaces, and environmental agents under various service conditions of the anticorrosion 2D coatings, and the contributions of individual microscopic factors and their couplings also require quantitative understandings. It is such insufficiency in the in-depth understandings of the microscopic mechanism that has made us short of principal guidance in property prediction and material design for better anticorrosion 2D coatings. As a highly accurate and efficient method, first-principles calculation based on density-functional theory (DFT) [16,17] is expected to be a powerful way to implement the prediction of the thermodynamic and kinetic properties of 2D coatings, as well as to understand the microscopic mechanisms for their corrosion behaviors. It is necessary for the current time to review the important progresses made by accurate first-principles calculations, which have revealed many essential atomic-scale mechanisms underlying the corrosion behaviors of Gr and h-BN coatings. Thus, such kinds of theoretical review can shed much light on the future research and development of these 2D coatings.

In DFT [18], the atomic structures, electronic structures, and physical properties of materials can be accurately calculated based on the principle of quantum mechanics, which allows the researchers to understand and design materials even without referring to the experimental information. Since the advent of DFT in 1964 [19,20], we have witnessed a

remarkable progress in DFT methods, as well as their applications. There have already been various prototypical versions of density functionals to describe electronic exchange-correlation potential on different levels of accuracy and efficiency (more accurate less efficient), e.g., local-density approximation (LDA) [21,22], semilocal generalized-gradient approximation (GGA) [23,24], metaGGA [25–28], and hybrid functionals [29–34]. Such a methodology hierarchy allows theorists to adequately study the complex thermodynamic and kinetic behaviors of anticorrosion 2D coatings using DFT by choosing the appropriate functionals with good accuracy–efficiency tradeoffs, based on which the relevant microscopic mechanisms (e.g., effects of defects, interfaces, and environmental agents) can be further analyzed in the DFT framework. Many originally calculated quantities, e.g., structural configurations, electronic structures, electronic energies, vibrational frequencies, and reaction paths and barriers, can be further processed to obtain various higher-level physical/chemical quantities and behaviors of materials, e.g., adsorption/binding energies, light absorption spectra, electron energy loss spectroscopy (EELS), Raman/Infrared spectra, scanning tunneling microscopy (STM) images, temperature-dependent reaction rate, and thermal desorption spectra (TDS), which can provide indispensable comprehensive information to understand the results from experimental observations, as well as to guide new experimental synthesis and characterizations. In short, the DFT-based first-principles approach, with its born advantages, can help us accurately and efficiently simulate the evolutions of material structures and properties, deeply reveal the microscopic mechanisms in the atomic scale and on the quantum-mechanics level, quantitatively explore the mode and strength of material–environment interactions, and reliably provide the guiding information for experimental design, synthesis, characterization, and material applications.

This review primarily focuses on the multiple factor coupling mechanisms for the corrosion behaviors of 2D coatings revealed by first-principles calculations, as well as on the promising optimization schemes guided by the in-depth and precise mechanism understandings. The corrosion resistance, physicochemical properties, and optimizations (e.g., bond-layer intercalation, surface modification, and deposition of corrosion-resistant oxides or inhibitor molecules) of 2D coatings on different metals are described. The critical roles of the structural defects in 2D coatings, coating–substrate interfaces, and environmental substances in such multiple-factor-coupled processes during the service of 2D coatings are evaluated. Finally, based on the existing research achievements, a prospective discussion is made on the future directions for developing better ultrathin 2D coatings.

2. Applications of 2D Materials as Anticorrosion Coatings

2.1. Anticorrosion Performance of 2D Coatings

The excellent corrosion and oxidation resistances of the Gr coating, due to its high air stability and excellent impermeability, have been extensively studied. In 2011, Chen et al. [35] used Gr to protect Cu and Cu–Ni alloys from oxidation and erosion in both air annealing (4 h, 200 °C) and liquid etchants (45 min, 30% H_2O_2). As Figure 1a shows, the photographs show the surface states of Gr-coated and -uncoated pennies and Cu foils after liquid etching and annealing. A significant color change of the uncoated samples indicates that the penny and Cu foil are severely oxidized, whereas the unchanged metallic color of coated samples demonstrates the superior protective performance of Gr as a passivation layer for metal. The uncoated Cu foil is detected by X-ray photoelectron spectroscopy (XPS) measurement to contain Cu_2O and CuO after the heat treatment, but no Cu_2O or CuO is detected on the coated copper foil. These experimental results clearly show that the Gr coating has protected the underlying Cu foil from oxidation and corrosion. Subsequently, Prasai et al. [36] employed electrochemical methods to assess the anticorrosion efficiency of Gr coating on Cu and Ni in aerated Na_2SO_4 solution. The measured cyclic voltammetry curves (i.e., cyclic potentiodynamic polarization curves, potential scanning rate 10 mV/s) have presented the remarkable suppression of many current-density peaks (associated with various redox reactions) by Gr coating, clearly indicating the considerable corrosion inhibition function of Gr coating. To quantitatively measure the corrosion potentials and rates of bare Cu and

Gr/Cu, their potentiodynamic polarization curves have been measured at a much lower potential scanning rate (0.005 mV/s) around the open-circuit potentials, and their Tafel analyses (Figure 1b) show that the multilayer Gr coating has reduced the corrosion rate of Cu by seven times and upshifted the corrosion potential by 25 mV. To further quantitatively evaluate the anticorrosion performance of the Gr coating, electrochemical impedance spectroscopy (EIS) can be adopted to derive some important electrical parameters of the coated surfaces under an oscillating potential around a given potentiostatic EIS potential (e.g., the open-circuit potential and a potential near 0 V [17,37]). The two most important electrical parameters for a coating (or a passivating film) intermediating the metal substrate and electrolyte are its Faradaic charge transfer resistance (R_{ct}) and its double-layer capacitance (C_{dl}). High R_{ct} and low C_{dl} values are usually characteristics of a good corrosion resistance of the protective coating because R_{ct} indicates the resistance to charge transfer across the coating during an electrochemical corrosion process and C_{dl} reflects the amount of water taken up by the coating surface. The obtained R_{ct} and C_{dl} of Gr/Cu are ~5 times larger and ~10 times smaller than those of the bare Cu sample, respectively, clearly showing the anticorrosion efficiency of the Gr coating on Cu [36]. The SEM images provide additional information about the nature of corrosion in Gr/Cu devices. The entire surface of the bare Cu is damaged after exposure to positive potentials, while most of the surface of the Gr-coated Cu is undamaged (Figure 1b).

Stainless steel has a high degree of significance in numerous industrial and civilian fields, due to its superior mechanical property, biological compatibility, and anticorrosion nature under various conditions. However, it has a poor anticorrosion efficiency in the strongly acidic environments (e.g., sulfuric, hydrochloric, and nitric acids), due to the instability of the involved transtion-metal elements and their passivating (hydr)oxide films against acid dissolution [38]. Impermeable 2D coatings can be used to solve such a corrosion problem of stainless steel in extreme corrosive environments, and Zhu et al. [39] has explored the anticorrosion efficiency of Gr coating on stainless steel. Comparing to the I–V polarization curve of bare stainless steel, the curve of Gr–steel is upshifted towards the higher potential by 20 mV, and the current is lowered by about 9 times (Figure 1c). Correspondingly, according to the corrosion rates derived from the polarization curves, the corrosion resistance of Gr-coated stainless steel is nine times of that of bare stainless steel. The optical images of bare stainless steel and Gr-coated stainless steel before and after electrochemical testing also display that the Gr coating has significant anticorrosion ability. The bare stainless steel is seriously corroded, while the stainless steel with Gr coating remains intact (Figure 1c). Furthermore, in an over six-year corrosion testing, few-layer Gr (FLG) protected Cu and confirmed the success of the long-term durable anticorrosion of Gr [40]. The low-magnification optical micrographs and SEM images of FLG and single-layer Gr (SLG) before and after the six-year ambient corrosion testing are shown in Figure 1d. The surface of Cu coated with FLG has no trace of oxidation under inspection with the naked eye, and there is more than one Gr layer on the Cu measured by SEM. On the contrary, the SLG-coated Cu's (SLG/Cu) surface turns into a dark color after the six-year environmental exposure, clearly indicating the occurrence of ambient oxidation and corrosion on SLG/Cu. The corresponding SEM image of SLG/Cu reveals many cracks existing in the SLG coating, which should be the weak points causing the failure of the SLG coating in anticorrosion. XPS and Raman spectra support the excellent antioxidation of FLG coatings (Figure 1d). A variety of Cu oxides and hydroxides (e.g., Cu_2O, CuO, and $Cu(OH)_2$) are detected on the SLG/Cu sample, while only elemental Cu is detected on FLG-coated Cu (FLG/Cu). The cracks on SLG/Cu will accelerate the localized corrosion owing to the galvanic coupling between the Gr coating and metal substrate [41]. Therefore, the FLG coating has a higher corrosion resistance due to the plugging/masking of the unavoidable structural defects in CVD Gr layers grown on metal substrates and the inhibited ingression diffusion of corrosive environmental agents.

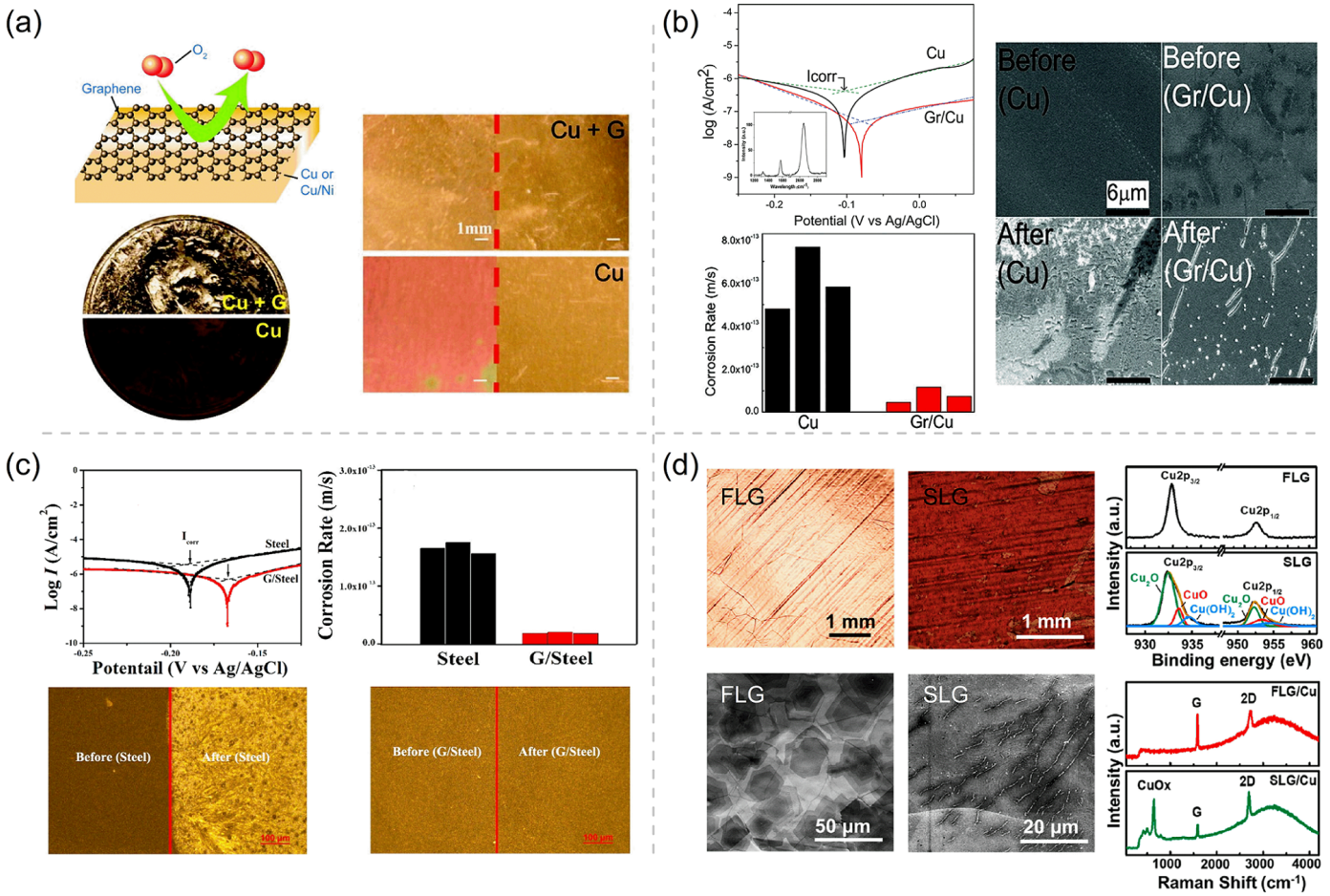

Figure 1. (**a**) Schematic depicting graphene (Gr) film as a chemically inert diffusion barrier, photograph showing Gr-coated and uncoated penny after 30% H_2O_2 corrosion, and photographs of Cu and Cu/Ni foils with and without Gr coating taken before and after annealing in air (4 h, 200 °C). Adapted with permission from Reference [35]. Copyright 2011, American Chemical Society. (**b**) Tafel plots and corrosion rates of Cu and Gr/Cu samples and scanning electron microscope (SEM) images of Cu and Gr/Cu sample before and after cyclic voltammetry (CV) scanning. Adapted with permission from Reference [36]. Copyright 2012, American Chemical Society. (**c**) Tafel plots and corrosion rates of bare stainless steel (labeled as steel) and Gr/stainless steel (labeled as Gr/steel) samples in 5% sea salt solution, and their optical images before and after the electrochemical anticorrosion testing. Adapted with permission from Reference [39]. Copyright 2016, American Chemical Society. (**d**) Optical and SEM micrographs of few-layer Gr/Cu (FLG/Cu) and single-layer Gr/Cu (SLG/Cu) after corrosion, and X-ray photoelectron spectroscopy (XPS) and Raman spectra of FLG/Cu and SLG/Cu. Adapted with permission from Reference [40]. Copyright 2021, American Chemical Society.

Without a protective coating, a bare metal surface will readily react with O_2 and H_2O. If a dense oxide film is spontaneously formed and can block the electron transport across the oxide film, the oxidant adsorption and ionic transport will be suppressed, leading to the corrosion/oxidation resistance of the native oxide film [42–44]. However, as a good conductor, the Gr coating will provide another electronic conduction path for the electron transport from metal to oxygen atoms, working as the cathode for the galvanic reaction and accelerating the corrosion of metal. The good dielectric properties and wide band gap of insulating h-BN can help avoid such electrochemical reaction on the metal surface, which protects the h-BN-coated metal from galvanic corrosion. Therefore, when the galvanic corrosion is to be avoided and a high surface conductivity is not required, the h-BN coating can be considered as a better alternative to Gr.

The barrier performance of h-BN is outstanding due to the similar structure to Gr and its insulating characteristics. Back to 2014, Li et al. [45] found that an h-BN nanosheet can effectively hamper the oxidation of the underlying Cu substrate after being heated

at 250 °C for 100 h. The heating of Cu with and without an h-BN coating generates the contrasting color changes of these two sample surfaces. The formation of black cupric oxide (CuO) and red cuprous oxide (Cu_2O) on the sample surface indicates that the Cu foil is oxidized. Under the same conditions, the h-BN-coated Cu foil retains much of its metallic luster, indicating a much lesser degree of surface oxidation, as shown in the optical microscopy photos (Figure 2a). In order to illustrate the corrosion kinetics of the Cu with and without an h-BN coating, the samples are permeated in N_2 gas bubbled 0.1 M NaCl solution for CV testing to obtain the current–voltage curves. According to the Tafel plots, the Cu with h-BN coating is corroded at a rate three times slower than that of uncoated Cu (Figure 2a). Zhang et al. [46] explored the anticorrosion performance of the 15 nm and 30 nm thin h-BN coating on Cu in Na_2SO_4 aqueous solution. The SEM morphology comparison of bare Cu, 15 nm h-BN-coated Cu, and 30 nm h-BN-coated Cu before and after the CV scanning is shown in Figure 2b. Pits and nano-sized particles appearing after scanning can be observed on all over the bare copper surface, with the particles having lower densities on the 15 nm and 30 nm h-BN-coated Cu than on the bare Cu. XPS measurements were carried out on bare Cu, confirming that those particles are $Cu(OH)_2$. Thus, such combination of SEM and XPS qualitatively prove the corrosion resistance of the h-BN coating. Tafel analysis and EIS analysis are used to quantitatively evaluate the passivating function of the h-BN coating, as shown in Figure 2b. The corrosion rate of h-BN-coated Cu is decreased by at least four times from that of bare Cu. From the magnitudes of $|Z|$ in the Bode plots, it can be seen that the electrochemical impedance of h-BN-coated Cu is 1.5 times and 5 times higher than that of bare Cu at low and moderate frequencies, respectively. Meanwhile, Shen et al. [47] compared the anticorrosion performance of h-BN and Gr, and confirmed the long-term corrosion resistance of monolayer h-BN for 160 days. Optical microscopy images of Gr/Cu and BN/Cu before and after 160 days of corrosion in the ambient environment are shown in Figure 2c. Compared with the Gr/Cu sample, the h-BN/Cu sample shows much less color change and less corroded areas, implying that h-BN rather than Gr is an effective long-term corrosion barrier for Cu. The Tafel plots and Bode plots of Gr coated Cu and h-BN-coated Cu both give out the same information as that from their optical microscopy images. h-BN-coated Cu has the lower corrosion rate (∼0.5 times) and higher electrochemical impedance (∼16 times) than those of bare Cu, while those of the Gr-coated Cu are slightly changed comparing to bare Cu (by ∼-0.07 times and ∼3 times, respectively), as shown in Figure 2c. The key mechanism for the excellent long-term barrier performance of the h-BN coating has been mentioned: The insulating nature of h-BN suppresses the galvanic corrosion. Chilkoor et al. [48,49] studied the ability of h-BN to suppress the sulfur corrosion that is usually caused by airborne sulfur dioxide and biogenic sulfide attack. The bare Cu, few-layer (∼4 atomic layers) h-BN-coated Cu, and multilayer (∼9 atomic layers) h-BN-coated Cu were exposed to planktonic cells for 27 days. The higher magnification SEM images after being exposed for 48 h and the corrosion rates for 27 days are shown in Figure 2d. After 48 h of exposure to planktonic cells, bare Cu suffers from an obvious biogenic sulfide attack, and multilayer h-BN-coated Cu is slightly corroded by microorganisms, while the few-layer h-BN-coated Cu retained its original metal shine. After the electrochemical testing, the corrosion rates and R_{ct} values of samples demonstrate that atomic h-BN layers reduce Cu corrosion by 2.5∼5-fold throughout the exposure period (Figure 2d). The corrosion rate of the multilayer h-BN-coated Cu is higher than that of the few-layer h-BN-coated Cu, because there is a higher degree of cell adhesion on the surface of the multilayer h-BN-coated Cu to produce a thicker biofilm.

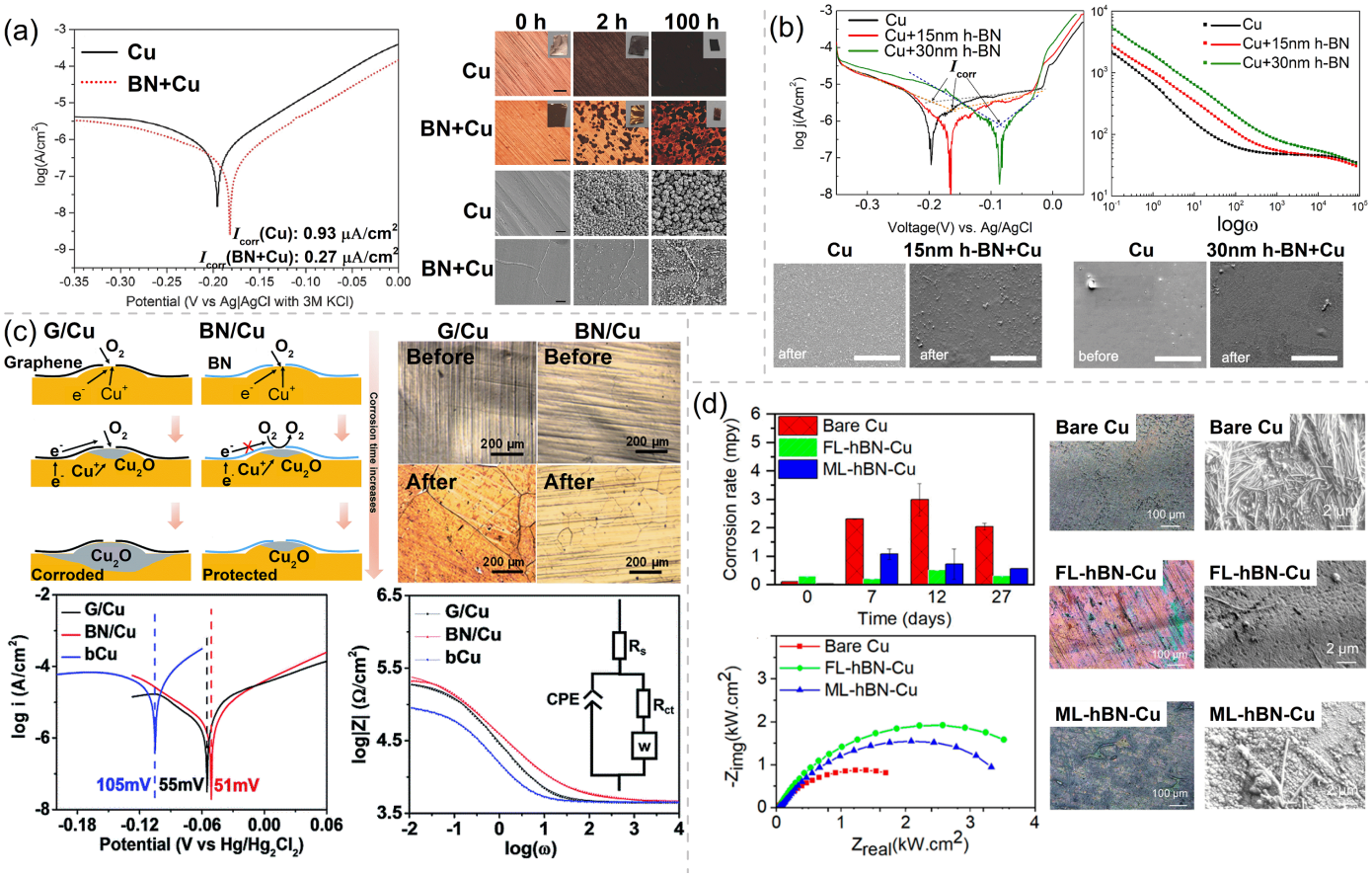

Figure 2. (**a**) The optical microscopy photos of the bare Cu and h-BN/Cu before (0 h) and after heating at 250 °C in air for 2 and 100 h and the Tafel plots of the bare Cu and h-BN/Cu in N_2-gas bubbled 0.1 M NaCl solution. Adapted with permission from Reference [45]. Copyright 2014, Wiley. (**b**) Tafel plots and Bode plots of uncoated Cu and h-BN/Cu samples in 0.1 M Na_2SO_4 solution and SEM morphology comparison of bare Cu, 15 nm h-BN/Cu, and 30 nm h-BN/Cu before and after corrosion testing. Adapted with permission from Reference [46]. Copyright 2016, IOP Publishing. (**c**) Schematic diagrams of the corrosion mechanisms for h-BN/Cu and Gr/Cu samples and optical microscopy images of Gr/Cu and BN/Cu before and after 160 days exposure to the ambient environment, and Tafel plots and EIS curves of bare Cu (bCu), G/Cu, and BN/Cu samples. Adapted with permission from Reference [47]. Copyright 2016, The Royal Society of Chemistry. (**d**) Corrosion rates and Nyquist plots of the bare Cu and h-BN/Cu exposed for 27 days and optical images and higher magnification SEM images of bare Cu, few-layer h-BN-coated Cu (FL-hBN-Cu), and multilayer h-BN-coated Cu (ML-hBN-Cu) before and after 48 h of exposure of planktonic cells. Adapted with permission from Reference [48]. Copyright 2020, American Chemical Society.

In order to systematically understand the corrosion resistance of 2D coatings, the experimentally measured corrosion rates and R_{ct} values of various coating–metal systems in different electrolytes are summarized in Table 1, where the 2D coatings grown by the same method (i.e., CVD) are focused. Due to the economical synthesis and possible massive application of CVD 2D coatings, this comparison may have much industrial significance for the research and development of 2D coatings in the future. As mentioned above, low corrosion rate values and high R_{ct} values may indicate the good corrosion resistance of coatings. However, the data in Table 1 show that although the corrosion rates of coated metal substrates are always lower than the corresponding bare metal substrates in the same experimental setups (i.e., corrosion inhibition efficiency $> 86\%$), the measured corrosion rates and R_{ct} values of both Gr and h-BN coatings on different metals (Cu, Ni, and stainless steel) do not exhibit any clear chemical trend. For example, the insulating h-BN coating (i.e., free of galvanic corrosion) is expected to have a higher corrosion resistance than the conducting Gr coating, while the as-synthesized CVD h-BN coating may surprisingly have a higher corrosion rate and a lower R_{ct}. This unexpected phenomenon for the short-

term corrosion may be related to the possible inferior morphology and quality of CVD h-BN coatings on metal substrates, which can be judged from many factors, e.g., the binding strength and the epitaxial relationship of the coating–metal interface, interface chemical stoichiometry, amount of coating defects (vacancies, grain boundaries, cracks, holes, and edges), and effective coverage of the flaky 2D coating on metal. This unexpected phenomenon also emphasizes the importance of a clear understanding on the microscopic mechanism for the multilateral coupling between the coating–metal interface, coating defects, and environmental agents, which especially needs DFT calculations.

Table 1. Corrosion rates (CR), corrosion-inhibition efficiencies ($\epsilon_{ci} = \frac{i_{bare} - i_{coat}}{i_{bare}}$), and R_{ct} values of various CVD 2D coatings grown on metal substrates in different electrolytes.

System	Electrolyte	CR (nm/s)	ϵ_{ci} (%)	R_{ct} (Ω/cm^2)	Ref.
Gr/Cu	Na_2SO_4	7.90×10^{-5}	86.38	1.01×10^4	[36]
Gr/Cu	5% sea salt	3.22×10^{-6}	93.55	-	[39]
Gr/Cu	0.1 M NaCl	1.14×10^{-3}	90.00	1.75×10^5	[47]
Gr/Ni	Na_2SO_4	1.70×10^{-6}	94.29	-	[36]
Gr/Ni	5% sea salt	2.42×10^{-5}	95.16	-	[39]
Gr/steel	5% sea salt	2.02×10^{-5}	88.45	-	[39]
Gr/steel	3.5 wt% NaCl	-	-	1.04×10^6	[50]
h-BN/Cu	0.1 M NaCl	1.46×10^{-3}	87.23	2.79×10^5	[47]
h-BN/Cu	0.5 M H_2SO_4	2.84×10^{-2}	93.03	-	[48]
h-BN/Cu	0.5 M Na_2S	1.65×10^{-4}	94.05	-	[48]
h-BN/Cu	planktonic cells	-	-	3.82×10^3	[48]

Recently, an experimental work on the short-term oxidation kinetics of Gr/Cu and h-BN/Cu has also well proven the changeable role of the coating–metal interface in determining the short-term oxidation path [51]. Ambient pressure photoelectron spectroscopy (APXPS) has been used to reveal the fully different oxidation mechanisms of Gr/Cu and h-BN/Cu in an isobaric O_2 atmosphere (2 mbar) heated at a constant rate (0.1 °C/s) from 50 up to 400 °C: (1) On Gr/Cu, the oxidation of Cu substrate (mainly into Cu_2O) follows the oxygen intercalation into the Gr/Cu interface; (2) On h-BN/Cu, the oxidation of Cu substrate (into Cu_2O and then CuO) follows the etching-off of h-BN coating. The Gr coating has a higher oxidation resistance than h-BN coating here, which is benefited from the protection function of the Gr/Cu_2O hybrid structure. However, during a long-term exposure to an oxidizing environment, when the exposed metal substrate areas are largely/fully passivated, the corrosion resistance of the h-BN coating will outperform that of the Gr coating as expected [47,52]. Galbiati et al. [52] have investigated the anticorrosion performance of Gr and h-BN coatings on Cu by using the real-time Raman and XPS characterizations in high temperature and long-term oxidative conditions. After being heated and exposed to the ambient environment for a long time, the Raman and XPS signal intensities for CuO, Cu_2O, and $Cu(OH)_2$ on the h-BN/Cu sample are extremely lower than those on the Gr/Cu sample, indicating that the h-BN coating has a superior corrosion resistance to the Gr coating in the high-temperature oxidative condition ($\geq$250 °C) and long-term working period ($\geq$9 h) [52].

2.2. Mechanical Performance of 2D Coatings with Similar Determinants

Apart from the aforementioned anticorrosion applications, the fascinating structural and mechanical properties of 2D coatings can bring other favored benefits to metal substrates, e.g., solid-state superlubricity and irradiation resistance, which can be used to reduce the tribological and irradiation damage of metal substrates [13]. Multilayer Gr and h-BN coatings, as well as transition-metal dichalcogenides (TMD), are perfect lamellar materials with weak physical interlayer interaction, making them excellent candidates to achieve superlubricity when coated on metal substrates. For instance, the friction coefficient of Gr/steel and h-BN/steel surfaces can be as low as ~0.04 and ~0.165, respectively, and

the friction coefficient of the hybrid coating made of Gr and h-BN can even be decreased down to 0.02 [53]. The hybrid Gr/MoS_2 and h-BN/MoS_2 coatings can further decrease the friction coefficient down to 0.01 because the special S–Mo–S trilayer sandwich structure can exclude the interlayer covalent–ionic bonding that occasionally happens in defective Gr and h-BN coatings [53].

The lubricating performance of 2D coatings depends on many factors, e.g., number of layers, coating–metal interfaces, coating defects, and working environments [54–59], which, in essence, is similar to the situation for the corrosion resistance of 2D coatings with multiple material–environment–anticorrosion relationships [36,40,48,60–67]. As the number of layers increases, the friction coefficient tends to decrease, e.g., the bilayer Gr coating shows a lower friction coefficient (by 67% on average) than that of a single-layer Gr coating, which is attributed to the higher degree of smoothness of the former coating [54,68]. The few-layer coatings can also have superior anticorrosion performance to the single-layer coatings, as mentioned in the above Section 2.1. When the Gr coating loosely binds with the metal substrate, the friction sliding may result in the puckering and deformation of the Gr coating in the out-of-plane direction due to the strong tip-Gr adhesion, leading to a high friction coefficient, as well as a possibly high tribocorrosion tendency in corrosive environments [54]. The strong Gr–substrate interface (e.g., on Ni, Pt, and mica) can not only give rise to a smooth surface and then to both the suppressed puckering and thickness dependencies, but it can also effectively prevent the environmental substances from entering into the coating–substrate interface [55,69,70]. For practical applications of large-dimension Gr coating (∼μm), the total friction force is dominated by contact edges and defects, which are also the weak points for the anticorrosion of coatings [56,69,71,72]. The dangling bonds at the edges and defects of a Gr layer will readily form covalent bonds with the surroundings Gr layers, resulting in the contribution (per atom) of edge atoms to the friction force being much greater (by 4–5 orders of magnitude) than that of inner atoms [56]. Furthermore, the environmental medium can readily have a great and fast impact on the coating lubricity, especially at the defects and edges of 2D coatings. For Gr and h-BN coatings, the dissociative chemisorption of water will passivate the dangling bonds at the defects and edges of 2D coatings, improving their wear resistance [57,58]. Meanwhile, for MoS_2, the friction and wear will increase as the environmental humidity increases, which may be due to the formed hydrogen bond (H–S) between water and MoS_2 and/or the wet oxidation of reactive defect sites in MoS_2 [59]. It can be found that whether it is the superlubricity or excellent corrosion resistance, the number of coating layers, the coating–substrate interface binding, the defects and edges of coatings, and the environmental substances are all key influential factors.

On the other hand, in strengthened Gr–metal composites, the Gr–metal interfaces can effectively enhance the radiation tolerance by removing interface dislocations, annihilating defects, hindering crack propagation, and reducing embrittlement [73]. The Gr additive usually plays a dominating role in reducing radiation damage, especially through enhancing the stability of grain boundaries and interfaces of the metal matrices. Currently, experimental methods are always used to reveal many macroscopic metallurgical properties and mechanisms, and some state-of-the-art theoretical calculations have helped in revealing many important microscopic mechanisms. Molecular dynamics simulations have confirmed that the Gr–metal interface can spontaneously absorb the nearby crystalline defects that are produced from a collision cascade, thereby enhancing the lifetime of the Gr–metal composites via this self-healing effect [74]. At the same time, the impermeability of the Gr layer to He gas can suppress the agglomeration of He gas into large bubbles [74,75]. It has been observed in an experiment that the defects created in Cu have a high migration speed towards the Gr–Cu interface, and an atomistic simulation further reveals that a large stress field exists at the Gr–Cu interface, and acts as the driving force for such fast diffusion and then annihilation of defects in the Gr/Cu composite [73].

2.3. Realistic Challenges of Anticorrosion 2D Coatings

Although 2D coatings may provide excellent protection for metals against environmental corrosion and oxidation, there still exist many inherent and technological challenges to overcome for the realistic applications of 2D coatings. The first challenge is caused by that the qualities of as-synthesized Gr and h-BN coatings never being good enough. The effective corrosion resistance of perfect Gr and h-BN coatings can be understood as a result of the extremely small pores ($\sim$0.06 nm^2) in their pristine hexagonal lattices, leading to the high impermeability [2,76–78]. However, the wrinkles, cracks, and defects of the single-layer coating caused by the chemical vapor deposition (CVD) growth are inevitable, and mechanical transfer declines or even deteriorates the the long-term corrosion resistance of Gr and h-BN. As Figure 3a shows, the metal oxides (e.g., Cu_2O, NiO, and Al_2O_3) formed by the reaction of metal with O_2 and H_2O can inhibit the transfer of electrons from the metal to the oxygen atoms, protecting the metal from corrosion. However, the contact between the Gr coating and the metal deteriorates the anticorrosion function of the metal oxide at the defect sites by providing an effective path for the electron transport. Thence, as shown in optical micrographs in Figure 3a, the corrosion of Gr-coated Cu is more severe than that of bare Cu [79]. Over a long period, many corrosive environmental agents (e.g., H_2O, O_2, and Cl^-) will infiltrate into the pinholes, cracks, and scratches on the coating, which is followed by the accelerated localized corrosion owing to the galvanic coupling at the coating–metal interface (Figure 3b) [10,36,41,60,79,80]. Although the h-BN coating is an insulator without galvanic corrosion, the grain boundaries and point defects can seriously influence its corrosion protection performance [45,48]. Grain boundaries and point defects in atomically thick h-BN layers can locally change their work function and are more reactive than pristine counterparts due to the unpaired π and σ electrons in the dangling bonds.

The second challenge is related to the fact that the anticorrosion efficiency of Gr and h-BN is partly determined by the substrate. Gr and h-BN can grow smooth morphologies on metal substrates (such as Ni or Co) that can strongly bond with these 2D coatings and have well-matched lattice constants, which is very conducive to the stable service of the coatings. On the contrary, bulges and wrinkles often appear on the surface of Gr and h-BN grown on many other metal substrates (such as Ru and Pt), which provide many easy ingression channels for corrosive/oxidizing environmental substances and endue considerable corrosion and oxidation under aggressive aqueous and high-temperature conditions, as well as damage the 2D coatings [13,81,82]. The extension of corrosion products underneath the weakly bound 2D coating may also readily lead to the cracking and spallation of the 2D coating. It has been realized that the coating–substrate interface's binding strength and the ability of metal substrate to form a passivating oxide film are the two keys for the 2D-material-coated metals to have long-term corrosion resistance [62]. Figure 3c illustrates the general model for 2D material passivation. The strong interaction between the Gr coating and the Ni/Co substrate (with a dense passivating oxide film) makes the Gr coating a superior long-term passivation barrier, whereas the Gr-coated Cu and Ir metals are reported to exhibit oxygen intercalation even under modest air exposures due to the weak inferface bindings therein [35,79,83–86].

The third challenge originates from the high complexity of the multiple-factor-coupling mechanisms for the chemical reactions of surfaces, interfaces, defects, and environmental substances, which still are not fully clear. Due to the multiple-factor coupling effect, it is difficult to stably control the coating preparation quality and corrosion resistance. The atomic-level thickness of the 2D anticorrosion coating brings great challenges to the experimental characterization to figure out the microscopic coupling mechanisms. Although many experiments have detected macroscopic corrosion resistance performance and microscopic states of materials by combining electrochemical polarization current methods and electron microscopy techniques (measurement of morphology and chemical composition), for the dynamic evolution of complex systems under multiple-factor-coupled environments, the academic community lacks accurate and systematic understanding of

quantitative contribution of various microscopic processes and the specific influence trends of individual environmental factors.

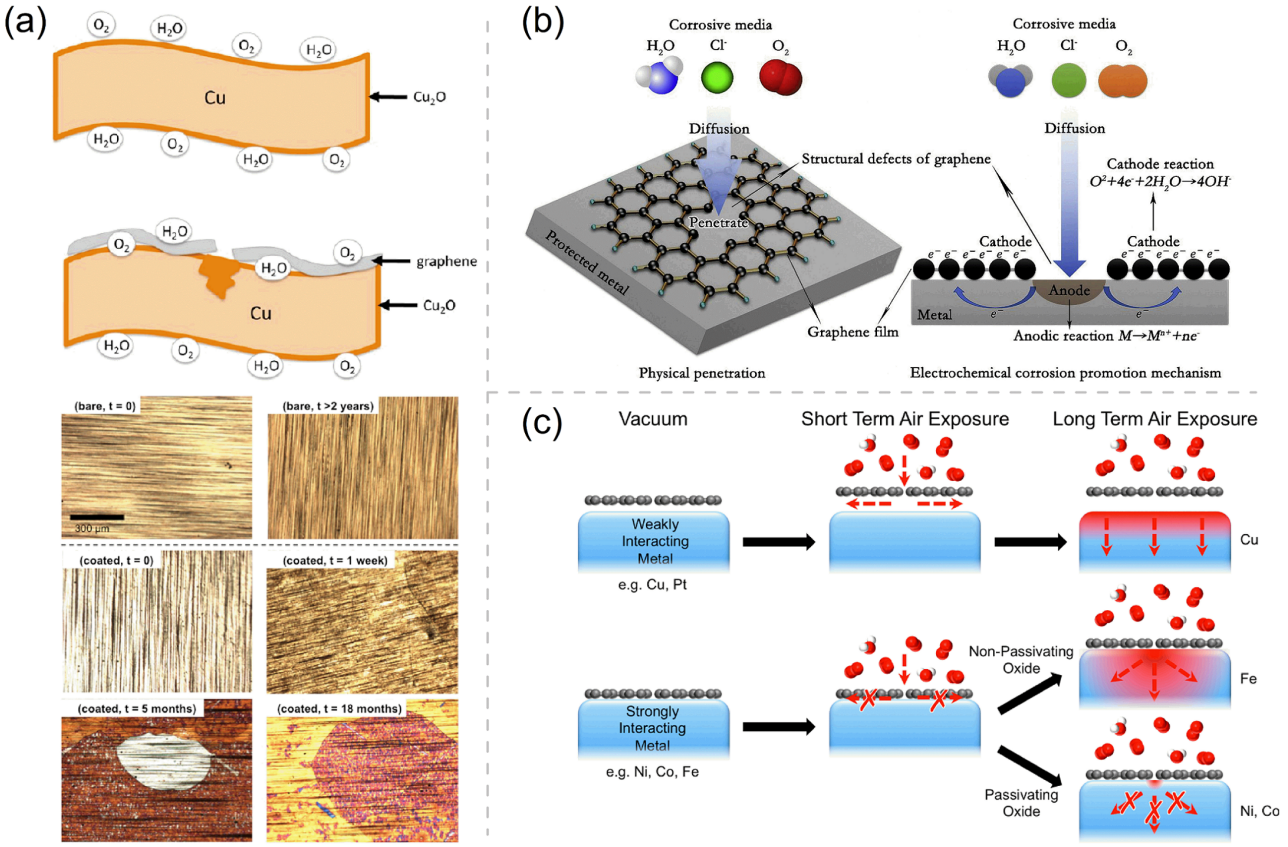

Figure 3. (**a**) The schematic of the oxide formation on bare and Gr-coated Cu, and the optical micrographs of bare and Gr-coated Cu foils before and after exposure to ambient conditions for 0 day, 1 week, 5 and 18 months, and 2 years. Adapted with permission from Reference [79]. Copyright 2013, American Chemical Society. (**b**) Schematic of galvanic corrosion occurring in the defects of pure graphene coating. Adapted with permission from Reference [10]. Copyright 2018, Elsevier. (**c**) Schematic showing the passivation function of different Gr-coated metals. Adapted with permission from Reference [62]. Copyright 2015, American Chemical Society.

2.4. Optimization Methods of Anticorrosion 2D Coatings

The above-mentioned challenges limit the practical performance and large-scale realistic applications of Gr and h-BN as the long-term passivating coatings in various aggressive environments. Several optimization methods have been studied to overcome the challenges and obtain a 2D coating with atomic thickness and superb long-term protection performance.

The first approach is to optimize the CVD preparation parameters and transfer methods to maximize the quality of the Gr and h-BN coatings with a reduced amount of structural defects on 2D coatings or to use multilayer Gr and h-BN coatings instead of their monolayer counterparts to reduce the risk of galvanic corrosion and localized corrosion at the defect sites. The CVD parameters, including growth time, hydrogen flow, cooling rate, and annealing temperature, can influence the defect density and corrosion resistance of Gr and h-BN coatings. The multilayer Gr with a long growth time has been proven to have better protection function for Cu [87]. A rapid cooling rate and absence of hydrogen flow significantly diminish the wrinkle formation and improve the durability of Gr coatings [88]. Heating CVD-grown monolayer Gr in air at 550 °C leads to the disappearance of wrinkles, nanoscale cracks and pits in the basal plane of the 2D-coating lattice [89]. These optimizing treatments all aim to adjust the coating–metal and coating–atmosphere interactions to ensure the integrity and flatness of the CVD Gr coatings. Many studies have proposed that multilayer Gr and h-BN coatings have better anticorrosion performance

than monolayer coatings, whether it is for short-term or long-term corrosion resistance. On the one hand, the multilayer coating (≥ three layers) effectively improves corrosion resistance by plugging/masking the defects of CVD Gr/h-BN grown on substrates and inhibiting the diffusion of environmental factors in the vertical direction [41,50,60,79,90]. The potential barriers of an O atom penetrating through the matched and mismatched eight-ring defects in the top and bottom atomic layers of the double-layer Gr coating are 3.55 eV and 3.38 eV, respectively (Figure 4a). On the other hand, the horizontal diffusion of environmental substances is inhibited by the barrier in the interlayer space within FLG coating [40,91], as shown in Figure 4a. The potential barrier for the diffusion of a water molecule into the interlayer space between two Gr layers is 2.5 eV, which is extremely high. The mechanical transfer process is easy to cause defects in 2D coating, and the multilayer Gr coating fabricated by mechanical transfer will unavoidably leave channels for the transport of corrosive agents and hence deteriorate the corrosion resistance of a mechanically transferred Gr coating on Ni, making it worse than the Gr coating grown directly on Ni by the CVD method [92].

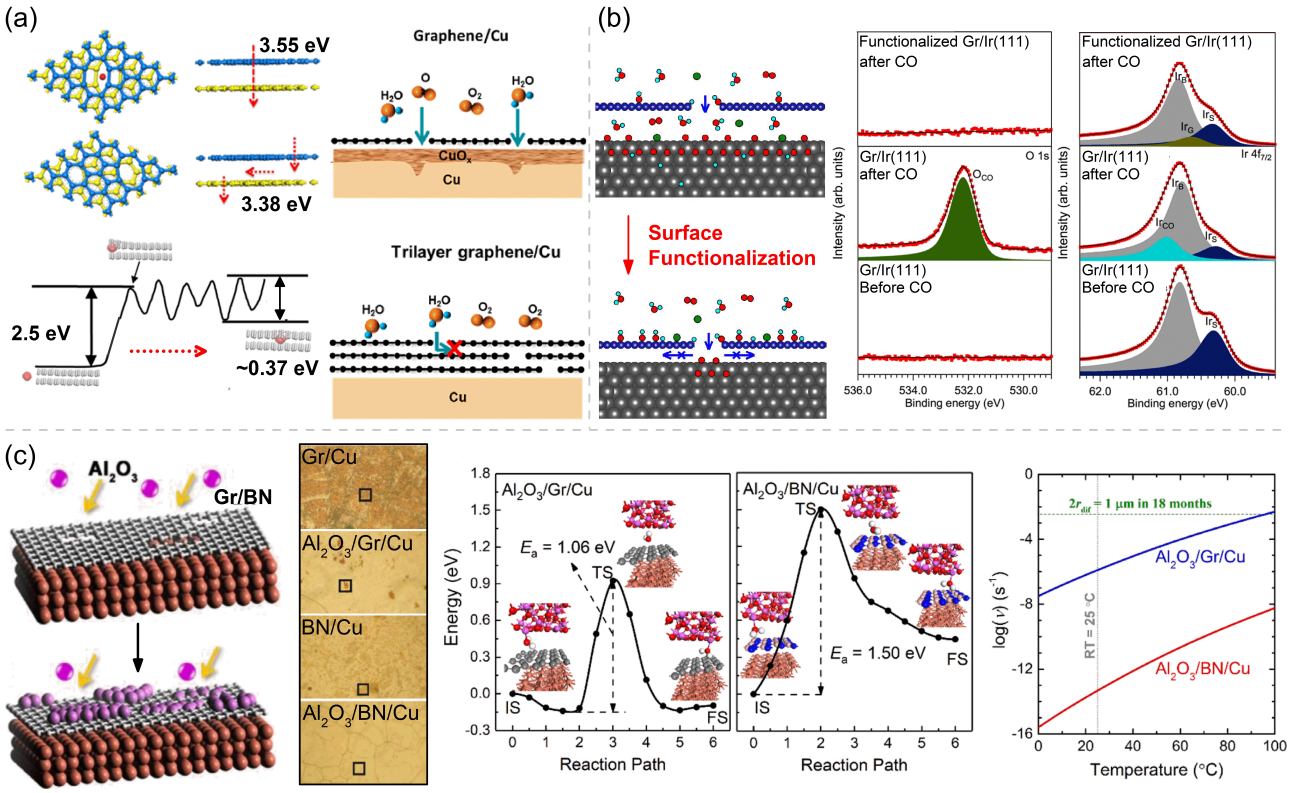

Figure 4. Various micro-control methods to improve the corrosion/oxidation resistance of 2D coatings: (**a**) DFT calculated potential barriers of an O atom permeating into the interlayer of double-layer Gr with matched and mismatched 8-ring defects (adapted with permission from Reference [91], Copyright 2018, Elsevier), schematics and calculated potential barriers for a H_2O molecule to diffuse through a defective double-layer Gr, and schematics showing the progress of reactive species to diffuse through single-layer Gr (SLG) and few-layer Gr (FLG)-coated Cu (adapted with permission from Reference [40], Copyright 2021, American Chemical Society). (**b**) Schematics of the progresses of reactive species to diffuse through weakly bound Gr–metal and strongly bound Gr–metal interfaces, and the XPS core-level spectra of clean Gr/Ir(111), CO intercalated Gr/Ir(111), and hydrogenated Gr/Ir(111) after exposure to 1 mbar CO at 473 K for 10 min. Adapted with permission from Reference [63]. Copyright 2018, American Chemical Society. (**c**) Schematics of Gr/Cu and BN/Cu surfaces before and after ALD-Al_2O_3 treatment, optical micrographs of Gr/Cu, Al_2O_3/Gr/Cu, h-BN/Cu, and Al_2O_3/h-BN/Cu (treated with 80 cycles of ALD) exposed to a humid air for 18 months, and reaction paths and energetic profiles for the diffusion of a H_2O molecule in Al_2O_3/Gr and Al_2O_3/BN interfaces and the temperature-dependent diffusion rate for these diffusion processes. Adapted with permission from Reference [90]. Copyright 2020, Elsevier.

The second anticorrosion optimization method is to increase the interaction between 2D coatings and different metallic substrates by surface modification. Kyhl et al. [63] functionalized the surface of monolayer Gr coating on the Ir(111) surface using hydrogen adsorption, which results in the newly formed chemical bonds at the Gr/Ir(111) interface and then the increased interface binding strength (i.e., shortened interface distance), as shown in Figure 4b. Exposing the Gr/Ir(111) surface to hot H atoms at 473 K yields a homogeneous hydrogen coverage with localized clusters of sp^3-hybridized areas, each of which contains the preferred C–Ir bonds. These C–Ir bonds shorten the distance between the Gr and Ir and suppress CO from entering the interface. The XPS spectra of the O 1s and Ir $4f_{7/2}$ core levels both show that CO obviously intercalates below a nonfunctionalized Gr coating and oxidized the underlying Ir(111) substrate, while the CO intercalation is fully blocked by the closely bound hydrogenated-Gr/Ir(111) interface (Figure 4b). Our theoretical calculations also reveal that the binding strength of Gr/Ni interface can be considerably enhanced by 0.37∼1.23 eV per covalent adsorbate (e.g., H, O, OH) on SLG or the buffer Gr layer in the multilayer coating [93].

The third anticorrosion optimization method is to deposit dense oxide nano-films on 2D coatings [94] to passivate the reactive structural defects on the Gr and h-BN coatings, which is a facile and efficient technique to enhance the barrier performance of Gr and h-BN. An atomic layer deposition (ALD)-deposited Al_2O_3 coating with a thickness of tens of nanometers has been proven to yield sufficient resistance to oxidation and corrosion. This coating can retard the oxidation reaction of Cu at 200 °C in air for 336 h, and greatly improve the corrosion resistance of Cu with the corrosion inhibition enhancement factor η = 97% [95,96]. Ren et al. [90] demonstrated that the Al_2O_3 deposition has a more prominent anticorrosion-enhancement effect on BN/Cu than on Gr/Cu. After being exposed to humid air for 18 months, most Cu grains of Gr/Cu have been heavily corroded, and some inhomogeneous corrosion patches also show on the h-BN/Cu. After being deposited with Al_2O_3, the corroded area of Al_2O_3/Gr/Cu is shrunk down to 5% of Gr/Cu, and the corrosion of Al_2O_3/h-BN/Cu is completely vanished (Figure 4c). This difference in anticorrosion efficiency is caused by the different deposition mechanisms of Al_2O_3 on Gr/Cu and h-BN/Cu. ALD-Al_2O_3 selectively passivates defects on Gr, while Al_2O_3 grows more uniformly on BN/Cu due to the stronger Al_2O_3-BN/Cu interface bonding. During an 18-month corrosion testing in the ambient condition, if a spatial dimension of 1 μm is set as the critical size to judge whether there is observable corrosion occurring at a surface spot, the required diffusion rate for corrosion occurrence can be derived to be larger than the critical ν_c = (3.5×10^{-3} Hz), which corresponds to a diffusion radius of 0.5 μn, as indicated by the green horizontal line in Figure 4c. However, the diffusion rates of H_2O in the interfaces between 2D coatings (i.e., Gr and h-BN) and Al_2O_3 deposits are much smaller than ν_c by 3 and 11 orders of magnitudes, respectively, at room temperature, indicating the high corrosion inhibiting function of the 2D coating/Al_2O_3 interfaces that are created by the ALD treatment. Therefore, ALD-deposited Al_2O_3 can not only passivate the reactive defects in Gr and h-BN coatings but can also form a strong interface with 2D coatings, both of which jointly contribute to the superior long-term corrosion resistance of modified Gr and h-BN coatings.

Although the anticorrosion optimization methods discussed above have been widely adopted in the scientific community, the 2D coatings have not yet been applied in practice on a large scale. Many shortcomings of the existing optimization methods (e.g., high cost, long and complex modification process, high technological requirements) are still the main factors limiting the development of 2D coatings. It is badly required in recent years to comprehensively establish the in-depth and quantitative understandings of the key microscopic mechanisms deciding the corrosion behaviors of 2D coatings and metal substrates. It not only can provide much guiding information to predict the process–structure–property relationships of 2D coatings in various service environments but also shed much light on the design of better 2D coatings with higher anticorrosion performance and lower technological/economical requirements. However, according to the above discussion, the

corrosion problems of 2D coatings involve the highly complex microscopic interactions between many atomistic material structures (e.g., interfaces, defects, surfaces) and multiple environmental agents (e.g., gases, solutions) under various conditions (e.g., heat, stress, acidity). This will definitely bring many technological, human-resource, and economical challenges to the experimentalists. Fortunately, DFT-based first-principles methods are by nature good at investigating such multiple factor coupling problems, and many individual atomic-scale microscopic mechanisms and their coupling effects can be accurately and efficiently explored, based on which we can make reliable predictions on the evolutions of material structures and properties under different environmental conditions and then provide indispensable guiding information for experimental preparations, characterizations, and materials applications [17]. In the following sections, we will focus on the recent achievements of DFT calculations on the related microscopic mechanisms for 2D coatings, as well as the possible exploitations of these mechanisms to improve the anticorrosion performance of 2D coatings, and finally discuss some theory-guided design schemes for new superior anticorrosion 2D coatings.

3. Multiple-Factor-Coupling Mechanisms Revealed by DFT Calculations

Both experiments and theoretical calculations reflect the great influence of structural defects and environmental substances on the corrosion resistance performance of 2D coatings grown on various metal and oxide substrates [61,63]. However, in recent theoretical studies using DFT, the coupling relationships between the coating–substrate interface, environmental substances, and structural defects are usually investigated separately. The multiple factor coupling nature of the corrosion problems requires us not only to reveal the effects of individual processes but also the methods and strengths of their couplings. Therefore, we will successively discuss below the binding of coating–substrate interfaces, the coupling between interfaces and environmental substances, and, finally, the multilateral defect–interface–environment interactions. This arrangement of contents may be helpful for us to fully understand the related issues in a simplicity-to-complexity manner, and stimulate more theoretical studies to develop more integrated DFT methods for such multiple-factor-coupled corrosion problems.

3.1. Binding of Coating–Substrate Interfaces

As mentioned in Section 2.1, strong interaction between 2D coatings and a metal substrate may make coating the superior long-term passivation barrier, whereas the 2D coating that weakly binds to the metal substrate only shows short-term anticorrosion performance. In order to obtain insight into improving the long-term passivation performance of 2D coatings through interface engineering, this section gives a general overview of the interfacial interaction, as well as its effects on the physical properties of 2D coating and metal substrate.

According to interface distance and binding energy, the Gr/metal and h-BN/metal interfaces can be categorized into two groups, i.e., the strong chemically bound interfaces (e.g., with metals such as Ti, Co, Ni, Ru, Rh, and Pd) and the weak physically bound interfaces (e.g., with metals such as Al, Cu, Ag, Cd, Ir, Pt, and Au) [13,97–119]. The interfacial interactions in Gr/metal and h-BN/metal systems are considered to depend on the number of *d*-electrons in the metals, the size of the atomic orbitals (determining the amount of orbital overlap across the interface), and the work function variance [120]. The interaction strength between the Gr coating and metal substrate can be reflected by the interface distances, the carbon solubility in metals, and the work–function difference between clean metal surfaces and pre-adsorbed Gr ($\Delta W = W_M - W_G$). Many theoretical results calculated by DFT for interface distances, carbon solubilities, and ΔWs are collected from the literature and listed in Table 2, which is convenient for comparison to reveal many important chemical trends. For the strong chemically bound interfaces, the Gr/metal and h-BN/metal interfaces have separations of around 0.21 nm, while weak physically bound interfaces exhibit interface separations of 0.33 nm, which clearly indicates the

determining van der Waals force therein. Generally speaking, the metals (except for Rh) with high carbon solubility (1.5∼6.0 at.%) tend to form strong chemical binds with Gr coating, and vice versa, the metals (except for Pt) with low carbon solubility (0∼1.5 at.%) are associated with weak physical binding with Gr. The difference between the calculated work function of clean metal surface and adsorbed Gr (ΔW) show the same trend. The strong chemically bound interfaces other than Gr/Ti always display a large ΔW (⩾1 eV), while the weak physically bound interfaces other than Gr/Pt have ΔW less than 1 eV. It is the fundamental covalent–ionic bonding mechanism between C and metal atoms that makes the structural/energetic trends of Gr–metal interfaces able to be indicated by the parameters of *d* electron number, carbon solubility, and work-function difference.

Table 2. The results calculated by DFT [13,97–104,106–117,119,121,122] for equilibrium distances of many Gr–metal interfaces ($d_{G/M}$), carbon solubilities (in at.%) in different transition metals at 1000 °C, work-function differences between clean metal surfaces and pre-adsorbed Gr ($\Delta W = W_M - W_G$), and equilibrium distances of the h-BN–metal interfaces ($d_{h-BN/M}$).

Metal	$d_{G/M}$ (nm)	Carbon Solubility (Atom%)	ΔW (eV)	$d_{h/M}$ (nm)
Ti	0.21	-	0.39	-
Co	0.21/0.33	3.41	1.66	0.21
Ni	0.21/0.33	2.03	1.81	0.21
Ru	0.21	1.56	-	0.24–0.37
Rh	0.22	0.89	-	0.20–0.44
Pd	0.23	5.98	1.64	0.23–0.30
Re	0.21	4.39	-	0.20–0.35
Al	0.34	0.03	0.18	-
Cu	0.33	0.04	0.82	0.32–0.38
Ag	0.33	0.01	0.68	0.28–0.34
Ir	0.34	1.35	-	0.22–0.37
Pt	0.33	1.76	1.26	0.23–0.33
Au	0.33	0.01	0.80	0.29–0.34

Due to the lattice mismatch, the interface configurations of the Gr/metal and h-BN/metal systems are different. The interface spacing can be determined by both many experimental techniques (e.g., high-resolution transmission electron microscopy (HRTEM) [123,124], intensity-voltage low-energy electron microscopy (LEEM) [125], X-ray standing wave (XSW) method [126], and total-reflection high-energy positron diffraction [127]) and DFT calculations [93,103,128,129]. Many studies have shown that the honeycomb lattices of Gr and h-BN have four different basic adsorption configurations on the matched metal–surface lattices (see Figure 5) [13,97,130]: (i) the atoms in 2D coatings are arranged on top of the triangular hollow sites of a metal surface; (ii) the coating atoms alternately occupy the sites above the metal atoms (metal-atop sites) and the "fcc" hollow sites (top-fcc); (iii) the coating atoms alternately occupy the metal-atop sites and the "hcp" hollow sites (top-hcp); and (iv) the bonds of the coating (C–C bonds or B–N bonds) lie above the sites between neighboring metal atoms, known as a bridge structure (top-bridge). For the h-BN coating, assuming we have a commensurate 1×1 overlayer structure on a metal substrate, i.e., zero lattice mismatch and no rotation, two distinct adsorption configurations (i.e., $B_{hcp}N_{top}$ and $B_{fcc}N_{top}$) with B and N on high-symmetry substrate sites are usually considered to understand the interface interactions. For the interfaces with 2D coating and metal substrate having considerable lattice mismatch between their unit cells, a rotation by 30° together with some lateral translating shift of atoms may help optimize the interface bonding with reduced lattice mismatch, e.g., the coating–Ag, coating–Au, and coating–Al systems [105,116,131]. Such supercelled lattice matching lead to the appearance of Moiré patterns frequently observed on many coating–metal systems, e.g., coating–Ru,

coating–Pt, coating–Ir, coating–Rh, coating–Au, and coating–Re [132]. It should be noted that even in the non-commensurate coating–metal pairs, which exhibit the aforementioned Moiré-like superstructures, the local atomistic interface configuration and chemistry can be well approximated by one of the above four basic unit-cell registries.

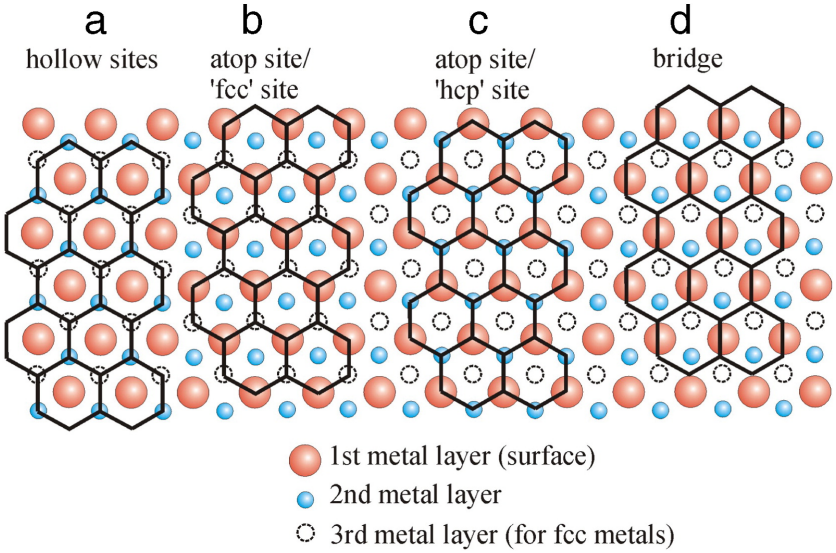

Figure 5. Four basic adsorption arrangements for non-rotated Gr on hexagonal (fcc(111) or hcp(0001)) metal surfaces: (**a**) hollow sites, (**b**) top-fcc sites, (**c**) top-hcp sites, (**d**) top-bridge sites. Adapted with permission from Reference [130]. Copyright 2012, Elsevier.

The binding mode between metal and Gr not only determines the interfacial configuration but also affects the electronic structure. For Gr, the strong covalent interaction at the chemically bound interface will break the sp^2-hybridized bonds of Gr, generate stable sp^3-hybridized states in the band structures of Gr, trigger a complete destruction of the Gr Dirac cone, and open a minigap of several meV at the Fermi level, which have been experimentally observed and theoretically confirmed on Gr on Ni(111) and Co(0001), as shown in Figure 6a [9,99,101,133]. In contrast, the weak interaction at the physically bound interface only involves a rigid Fermi level shift owing to the charge transfer at the interface and the resultant dipolar electrostatic field across the interface, which is closely determined by ΔW. For example, Au and Pt will induce the *p*-type doping of the adsorbed Gr coating, making the Dirac cone point higher than the Fermi level, while Al and Cu will lead to the *n*-type doping with the Dirac cone point lower than the Fermi level (Figure 6a) [99,100,120,134]. The significant effect of strong chemical interface bonding can also be clearly observed from the electronic structures of h-BN–metal systems. Pristine h-BN is an insulator with a wide band gap of 4 eV. However, when h-BN forms chemical interfacial bonding with a metal surface, this insulating character will be totally disappear, and many conducting Fermi-level electronic states will be created in the band structure of the adsorbed h-BN [115,116]. This can readily seen from the electronic densities of states for the h-BN/Co, h-BN/Ni, h-BN/Rh, h-BN/Ir, h-BN/Pt, and h-BN/Au systems, as shown in Figure 6b.

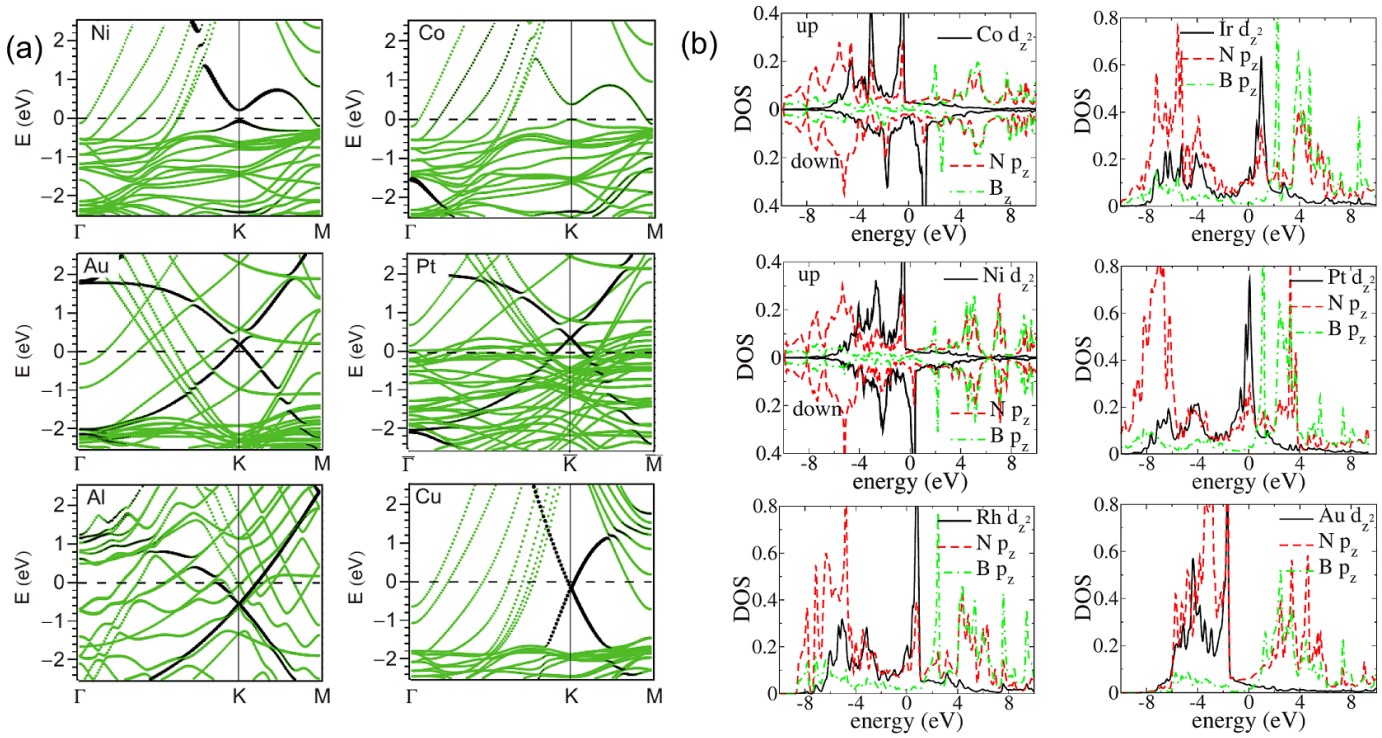

Figure 6. (**a**) Band structures of Gr adsorbed upon the (111) surfaces of Ni, Co, Au, Pt, Al, and Cu. Adapted with permission from Reference [99]. Copyright 2009, American Physical Society. (**b**) Electronic densities of state (DOS) of h-BN adsorbed upon Co, Ni, Rh, Ir, Pt, and Au. Adapted with permission from Reference [115]. Copyright 2008, American Physical Society.

3.2. Coupling between Interfaces and Environmental Substances

The structural defects in 2D coatings cannot be avoided during the CVD growth process and transfer process. Thereby, the anticorrosion performance and lifetime of Gr and h-BN coatings largely depend on the interaction between metal exposed by defects and environmental substances. The adsorptions of environmental radicals (e.g., H, O, OH) around coating defects after the dissociation of O_2 and H_2O molecules are always the precedent reaction steps for the continuous oxidation and corrosion processes happening on alloy substrates. Shortening the interface distance between the 2D coating and the metal can slow down the migration rate of environmental substances to the defect and then delay the corrosion process at the defect sites to a certain extent. For pristine Gr and h-BN coatings on metal substrates, the bonding strength of the interfaces, which decides the interfacial distances, is an inherent physical property and is only related to the types of coatings and metals. On the other hand, the adsorption strengths of molecules or atoms on free-standing Gr and h-BN layers are usually very weak, with adsorption energies ranging from several dozens to hundreds of meV. Thus, the adsorbates always have high migration rates on Gr and h-BN surfaces. Fortunately, recent theoretical studies using the first-principles approaches have demonstrated that metal-supported Gr and h-BN coatings can strongly adsorb certain environmental substances and reduce their migration rates on the coating. At the same time, the binding energies of 2D coating–metal interfaces also are increased by the adsorptions of environmental substances [93,105,135,136]. Engineering the adsorption affinity of environmental substances on metal-supported 2D coatings is a low-cost and easy-to-implement method to improve the oxidation and corrosion resistance of the 2D coatings. It only needs to maintain the sample in elaborately prepared atmosphere or solution for a period of time, which can allow the preferred adsorption reaction to happen [63]. However, the success of this engineering technique requires a systematic and in-depth understanding of the complex coupling between the adsorbates and underlying 2D-coating–metal interfaces. In this section, the interactions between the 2D-coating–

substrate interface and environmental substances revealed by DFT are introduced, and the adsorbate–interface coupling mechanism is summarized.

Among various Gr–metal and h-BN–metal systems, Gr/Ni and h-BN/Ni are important prototypes because they not only possess some favored intrinsic physical properties (e.g., small lattice mismatch and interfacial binding) but also have profound significance in the synthesis of Gr and h-BN sheets and the applications of Ni-based metals in aggressive environments. In addition, the two binding states (i.e., chemical and physical binding states) of the Gr/Ni interface are very close in binding energy, with a marginal difference of just 5 meV per C atom. This indicates that both binding states can coexist in regular realistic thermal conditions if there is not any biasing external perturbation (e.g., adsorption of environmental species) [93,137,138]. The transition process from physical binding state to chemical binding state can be used in theory to probe the effectiveness of a surface modification method [93]. The conclusions obtained from Gr/Ni system can also be readily generalized to other chemically bound or physically bound Gr–metal systems.

Sun et al. [93] investigated the binding strength of the Gr/Ni interface, the stability of atmospheric adsorbates (e.g., H, O, OH, and H_2O) on both monolayer and multilayer Gr coatings, and the adsorbate–interface coupling mechanisms using DFT calculations (Figure 7a). To investigate the mutual coupling between the atmospheric adsorbate and the Gr/Ni interface, the interface binding energy (E_b) of Gr/Ni and the adsorption energy (E_a) of the adsorbate on Gr coatings are calculated. E_b is defined as the electronic-energy difference between the states after and before interface binding, expressed as:

$$E_b = E_e(\text{X@Gr/Ni}) - E_e(\text{X@Gr}) - E_e(\text{Ni}), \quad (1)$$

where E_e is the total electronic energy, and Ni, X@Gr, and X@Gr/Ni represent the structural models of the Ni substrate, the Gr coating with an adsorbate X, and the Gr/Ni with an adsorbate X, respectively. Similarly, E_a is defined as the electronic-energy difference between the states after and before adsorption, expressed as:

$$E_a = E_e(\text{X@Gr/Ni}) - E_e(\text{X}) - E_e(\text{Gr/Ni}). \quad (2)$$

Furthermore, the diffusion mobility of the adsorbate is also calculated to reveal the effect of adsorbate–interface coupling on the kinetic properties. The diffusion barrier (E_{ac}) is defined as the electronic-energy difference between the transition state and the stable state. The temperature-dependent diffusion rate (i.e., jump frequency) is calculated using the transition-state theory [139], which is expressed in an Arrhenius form as:

$$\nu = \nu^* \cdot \exp\left(-\frac{E_{ac}}{k_B T}\right), \quad (3)$$

where k_B and T are the Boltzmann constant and the temperature, respectively, and ν^* is the prefactor and depends on both the temperature and vibrational frequencies at the initial stable state and transition state.

Adsorbates (e.g., H, O, OH), which can form strong covalent bonds with a Gr coating tend to significantly lower the binding energies of the chemically bound Gr/Ni interface by 1.0∼1.5 eV and shorten the interfacial distance by ∼0.95 Å [93]. Reducing the interface distance can suppress adsorbates from entering the interface and corroding the metal, improving the corrosion resistance efficiency of the coating. The E_as of H, O, and OH adsorbates on Gr/Ni also are increased by 1.2∼1.6 eV. The strong coupling between the Gr/Ni interface and covalent adsorbates significantly increases the diffusion barriers of H and OH adsorbates on Ni-supported Gr by 0.66∼0.93 eV and decreases the room-temperature diffusion rates of these adsorbates on the Gr surface by 10^{11}∼10^{16} times. These data indicate that the decomposition products of water (H and OH) adsorbed on the Gr surface can be inhibited by the substrate Ni from their migration towards the defect sites, thereby greatly ameliorating the long-term anticorrosion performance of the Gr coating. Unfortunately, H_2O, which is physically adsorbed, has negligible effect on the Gr/Ni

interface's binding strength and interfacial distance. In order to avoid the galvanic corrosion processes, multilayer Gr coating is used more frequently in practical applications to cover defects on Gr. Sun et al. [93] calculated the adsorbate–interface coupling of adsorbates on different locations of multilayer Gr coating grown on Ni, revealing that only adsorbates which are adsorbed on the buffer Gr layer have the strong coupling with the Gr/Ni interface, and proving that multilayer Gr coating has a better barrier performance than monolayer Gr due to the chemical inertness of the upper Gr layer. The dramatic adsorbate–interface coupling occurs with the covalent adsorbates (O, H, and OH) on the monolayer Gr coating or the buffer Gr layer in multilayer coating, while the physical adsorbate H_2O has a negligible effect on the Gr/Ni interface. This phenomenon uncovers the key to the adsorbate–interface coupling: The covalent adsorbate–Gr bonding results in unpaired π electrons that turn to enhance both the interface binding and adsorbate stability [93]. H_2O with a large HOMO-LUMO gap requires a significant energy cost to exchange electrons with Gr, resulting in its very weak physical binding on Gr even with the support of Ni. Contrary to the adsorption of H_2O, the chemical adsorption of molecule O_2 can be activated by the Ni supported Gr with an adsorption energy of -3.22 eV, compared to the adsorption energy of just -0.07 eV for O_2 on free-standing Gr [140]. This calculation result complements the mechanism discussed above: The sufficient amount of unpaired π electrons of Gr generated by interface bonding or atomic/radical adsorption can play a very important role in the adsorbate–interface coupling.

Similar to the adsorbate–interface coupling mechanism of Gr, the Ni support also strongly affects the chemical properties of monolayer h-BN. The adsorption energies of NO_2 and O_2 molecules have also been found to be increased from 0.025 and 0.032 eV on free-standing h-BN, respectively, up to 1.414 and 1.725 eV on Ni-supported h-BN, and the distance of h-BN/Ni interface is also decreased from 3.2∼3.6 AA down to ∼1.5 Å by the adsorptions of NO_2 and O_2 [135,141]. These energetic and structural changes clearly indicate that both the adsorbate–h-BN bonding and h-BN/Ni interface interactions have remarkably changed from a weak van dar Waals type into a strong covalent-ionic type. The NO_2 and O_2 molecules have moderate HOMO-LUMO gaps of 2∼2.5 eV, which are not easy to destroy and explains their weak adsorption on pristine h-BN, while the strong chemical coupling between these adsorbates and the h-BN/Ni interface can considerably change the HOMO and LUMO states (Figure 7b), leading to the largely enhanced adsorption. On the other hand, the adsorbed molecules such as N_2O and H_2O have very large HOMO-LUMO gaps of ∼6 eV, thus their electronic states are hardly changable by the Gr/Ni interface, resulting in their very weak physical adsorption (Figure 7b). Although the NO molecule has a quite low HOMO-LUMO gap of ∼0.5 eV, its LUMO state has a spin-down polarization reverse to the major spin-up direction (e.g., of the Ni substrate and the HOMO state of NO), thus, the electron transfer from the spin-up h-BN/Ni onto the low-lying spin-down LUMO state of NO is fully forbidden in principle. The spin-up LUMO lies at a very high level ($\gtrsim$6 eV) above the spin-up HOMO, and it is such a large spin-up HOMO-LUMO gap that leads to the weak physical adsorption of NO on h-BN/Ni (Figure 7b) [135,141]. In addition to molecules such as NO_2 and O_2, the changes in the adsorption energy and the adsorption site of O and OH on h-BN by the supporting Ni can also highlight the strengthening of adsorbate–coating bonding by the interaction between the h-BN coating and the Ni substrate. The O adatom bridges N and B atoms on the free-standing h-BN with a calculated E_a of -1.67 eV, while the O adatom bridges two B or two N atoms on h-BN/Ni with a considerably enlarged E_a of -3.35 eV. The OH adsorbate is adsorbed on top of a B atom on both h-BN and h-BN/Ni, with the corresponding E_as of -0.71 and -3.23 eV, respectively [141,142].

This adsorbate–interface coupling mechanism indicates that the binding states of Gr/Ni and h-BN/Ni can be engineered in a quite facile way through the surface modification of Gr and h-BN coatings by various environmental adsorbates, which have profound importance for the potential applications of corrosion-resistant Gr and h-BN coatings. The microscopic mechanisms can also motivate various following studies about many kinds

of adsorbates and Gr–metal systems. There has existed an experiment to prove that this surface modification can increase the protection of Ir metal by Gr coatings. Kyhl et al. have shown that the strengthened Gr/Ir(111) interface after hydrogenation can effectively prevent the intercalation of oxidative CO molecules in the millibar range of gas pressure. The scheme leads to protection against at least 10 times higher pressure and 70 times higher influences of CO compared to the protection offered by pristine Gr/Ir(111) [63].

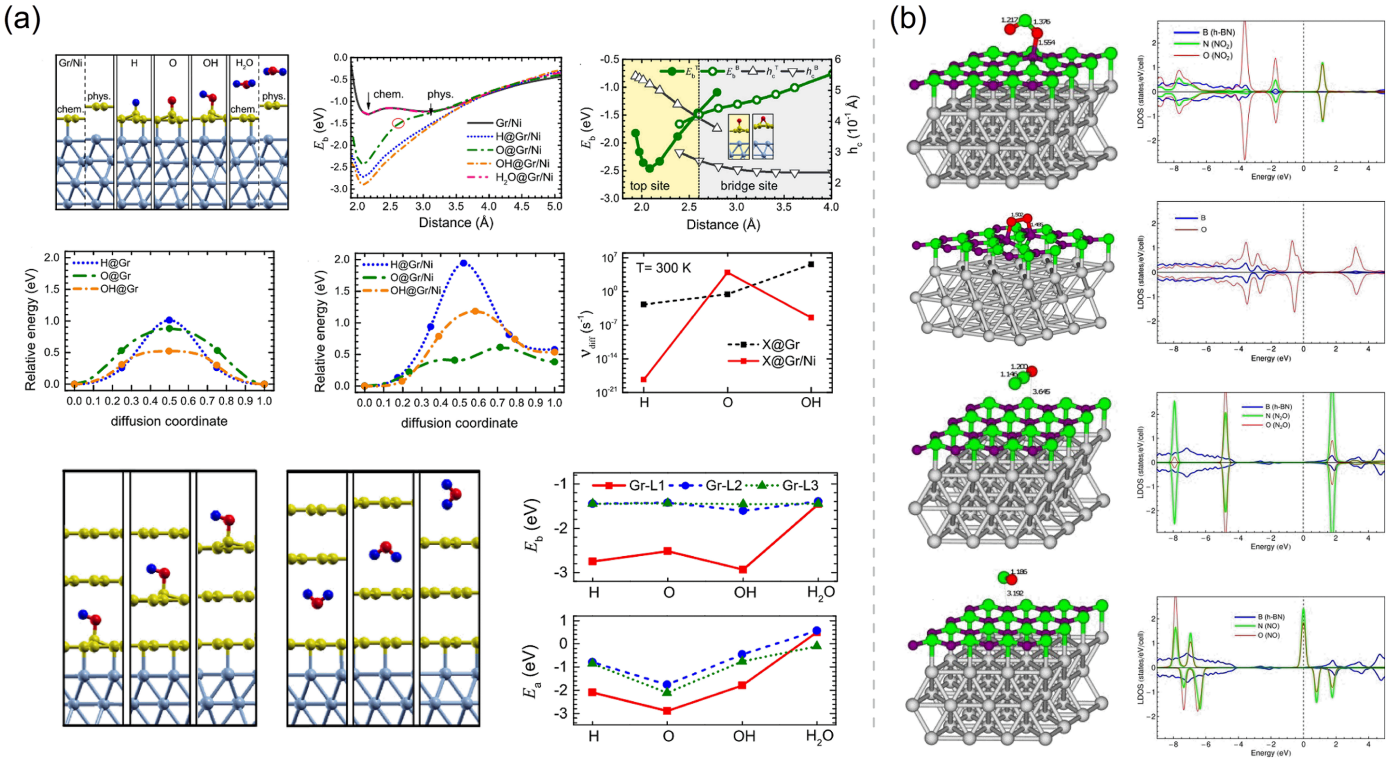

Figure 7. (**a**) Optimized structures, interface binding energies (E_b), adsorption energy (E_a), minimum energy paths for the diffusions, and diffusion rates of adsorbates (H, O, OH, H_2O) on monolayer Gr/Ni and trilayer Gr/Ni. Adapted with permission from Reference [93]. Copyright 2021, Elsevier. (**b**) Optimized structures and calculated spin-resolved projected density of states of NO_2, O_2, N_2O, and NO on h-BN/Ni(111). Adapted with permission from Reference [135]. Copyright 2014, Elsevier.

3.3. Multilateral Defect–Interface–Environment Interactions

Defects in the sp^2-hybridized sheet can play a critical role in the adsorbate–interface coupling interaction. The defects may be single atomic defects or an array of defects that form an extended structure. The unsaturated C, N, and B atoms at the lattice vacancies can form strong covalent bonds with the surface metal atoms underneath the defect edges, even if the metal is physically bound with the Gr and h-BN coatings. The unpaired π and σ electrons from the dangling bonds at the defects participate in the electron transfer and chemical bonding across the coating–substrate interface. DFT studies have shown that point defects dramatically change the interface structure and highly enhance the binding strength between two materials [143–146].

For Cu-supported Gr with single vacancy (SVG/Cu), the dangling bonds on the C atoms around the vacancy are saturated by forming three C–Cu bonds (bond length 1.94 Å), with the Cu atom right below the vacancy being pulled slightly out of the surface. For SVG/Pt, the C atoms around the vacancy form two C–Pt bonds (bond length 2.02∼2.21 Å) due to the lattice mismatch (Figure 8a) [143]. For SVG/Ni, three unsaturated C bonds strongly interact with the underlying Ni atoms, and the length of the C–Ni bond is only 1.87 Å [144]. The point vacancies in the Gr coating significantly increase the interfacial binding strength (associated with the lowered binding energy and shortened interface

distance) and the bucklings of both the Gr coating and the metal surface (caused by the interface atomic bonding) [146]. For Al-supported h-BN with single vacancy (SVh-BN/Al), it is illustrated that while N vacancies (V_N) do not give rise to any sizable strengthening effect on the h-BN/Al interface, B vacancies (V_B) interact strongly with the Al substrate. The reactivity of B atoms at the edge of V_N is much weaker than that of N atoms at the edge of V_B. The N atoms around V_B have more unpaired π and σ electrons and lower electronegativity than the B atoms around V_N, thus the covalent–ionic bonding of the N atoms with the metal substrate will be stronger. The highly reactive N atoms with dangling bonds can essentially "pull out" the underlying Al atom from the surface, as shown in Figure 8b [145].

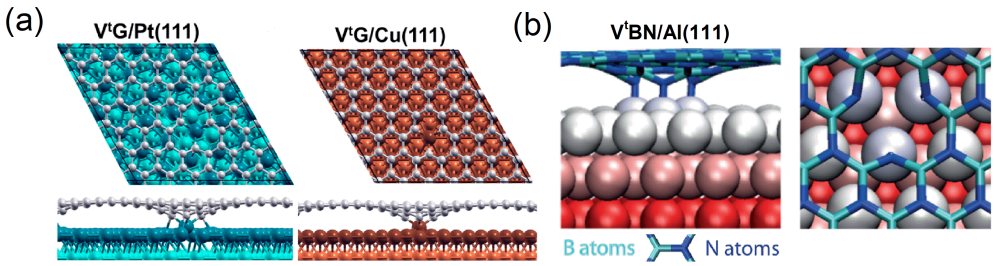

Figure 8. Top and side views of the structures for (**a**) Gr coating with point defect adsorbed on Pt (111) and Cu (111) substrates (adapted with permission from Reference [143], copyright 2017, American Chemical Society) and (**b**) h-BN coating with point defect adsorbed on Al (111) substrates (adapted with permission from Reference [145], copyright 2014, American Chemical Society).

The strong C–metal or N–metal covalent bonds may also be easily broken by the adsorbates (e.g., CO, O_2, OH and H). The thermodynamic calculations using DFT by Ferrighi et al. [143] have indicated that the dissociation of H_2O can readily occur on the SVG/Cu, and the surface of defective Gr coating keeps a quite high reactivity for such reaction though the dangling bonds at V_C have been saturated by the Cu substrate prior to the H_2O adsorption. As Figure 9a shows, the dissociation of an adsorbed H_2O molecule on the surface of SVG/Cu leads to stable the adsorption of decomposed products (i.e., one O and two H adatoms) on SVG. This adsorption–dissociation process acquires the breaking of existing Cu–C bonds and the formation of new C–H and C–O bonds around the V_C in the SVG coating, with the O adatom binding with two of the unsaturated C atoms of V_C and both H adatoms binding with the remaining unsaturated C atom. Similar to the dissociation of H_2O on SVG/Cu, the chemisorption of CO on SVG/Cu (and SVG/Ni) also breaks three C–Cu (C–Ni) bonds, which pushes the protruded Cu (Ni) atoms in SVG/metal back into the surface basal plane [144]. On the contrary, the SVG/Pt interface has a very low chemical affinity to H_2O. H_2O molecules in the environment will most likely be physisorbed on SVG/Pt rather than have chemical reactions with a V_C on the surface. It is the strong C–Pt bonds in defective-SVG/Pt that have lowered the reactivity of V_C with H_2O, resulting in the suppressed chemisorption and dissociation of H_2O (Figure 9b). From these examples, it can be readily found that the V_C-substrate bonding with the V_C-adsorbate bonding compete with each other in the SVG–metal systems. Strong C–metal bonds can prevent the chemisorption and dissociation of H_2O and then will not widen the interface spacing, which will not allow the corrosive environmental substances to extend underneath the defective 2D coatings.

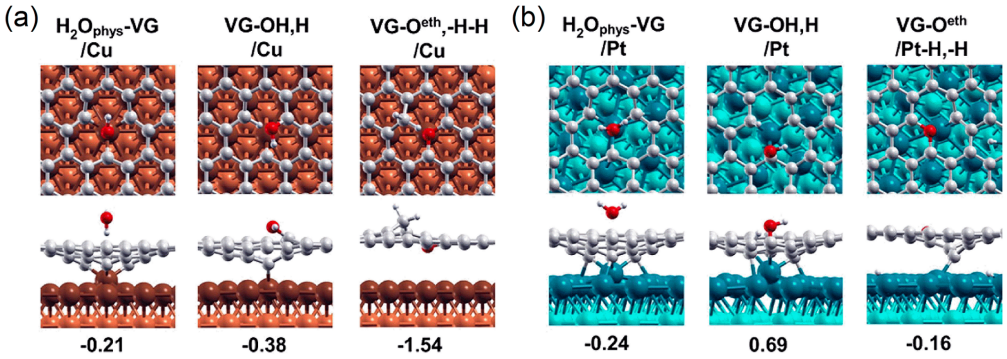

Figure 9. The calculated dissociation paths of a H_2O molecule on (**a**) defective-Gr/Cu and (**b**) defective-Gr/Pt surfaces, where three key steps are presented by the top and side structural views. Adapted with permission from Reference [143]. Copyright 2017, American Chemical Society.

4. Guided Engineering of Defects and Interfaces

The clear understanding on the complex coupling mechanisms between coating–metal interfaces, coating defects, and environmental substances can provide much guiding information for the design of new methods to improve the anticorrosion function of 2D coatings, e.g., by effectively engineering the properties of interfaces and defects.

First, since the strong coating–metal interaction is the key to achieving long-term passivation, due to the prevented intercalation and diffusion of oxidative and corrosive environmental substances in the coating–metal interfaces, the metals (e.g., Ni, Ti, Co, Ru, Rh, Pt, Re) that can chemically bind with 2D coatings are more preferred to support Gr and h-BN coatings. For the physically bound coating–metal interfaces, depositing on the matrix-metal surface with a bond-layer Ni metal should be an effective choice to improve the adsorption stability and anticorrosion function of 2D coatings because of the resultant strong chemically bound interface and the small lattice mismatch between Ni and the Gr/h-BN coating. This bond-layer approach can also help to decrease the appearance of bulges and folds produced during coating synthesis, thermal treatments, and applications [147].

Furthermore, oxide films natively formed on metal surfaces can also be used as an adhesive bond layer to support 2D coatings. Jo et al. [148] have found that the as-grown CVD Gr coating can provide a better corrosion protection for the Cu substrate than the natively formed oxide film on bare Cu during a period within 8 days, while the corrosion is accelerated by the CVD Gr coating during the long-term corrosion tests (>8 days) due to the unavoidable defects and existing galvanic-cell effect. However, if the Gr is wet transferred onto the Cu substrate, where the metal surface is pre-oxidized by water, the superior long-term anticorrosion can be realized, and the corrosion resistance is two times higher than the uncoated Cu [148]. The protection effect of 2D coatings on the oxide bond layer may be more important for some highly reactive metals (e.g., Mg, Li) because their native oxide films (e.g., MgO, Li_2O) also are not electrochemically stable if not protected. However, these oxides can provide some passivating effect due to their insulating character and the inhibited mass migration across the oxide film, the suppression of the galvanic-cell effect between Gr coating and metal substrate, and may also have good adhesion with 2D coatings due to the abundant dangling bonds on oxide surfaces. Shang et al. used Gr coating to effectively cover the defective oxide film natively grown on a Mg alloy (AZ91 Mg alloy, with 9.4 wt.%Al, 0.82 wt.% Zn, 0.23 wt.%Mn, 0.02 wt.%Cu, 0.01 wt.%Si, 0.005 wt.% Fe, 0.002 wt.% Ni), and successfully reduced the corrosion rate of an AZ91 alloy by 1∼2 orders of magnitude [149]. In addition to selecting a suitable substrate and bond-layer, the 2D coating can also be surface modified based on the adsorbate–interface coupling mechanism to enhance the interface binding strength (e.g., Gr/h-BN hydrogenation) [63].

Second, for the purpose of preventing corrosion and oxidation substances from being introduced into the interface through defects, depositing corrosion-resistant dense oxides (e.g., Al_2O_3, ZnO, NiO, Cr_2O_3, and TiO_2) and some corrosion inhibiting molecules on 2D coatings will be an efficient and economic approach. The deposited oxides and inhibitors

will selectively passivate the defects on 2D coatings and hinder the passage of corrosive environmental substances. Hsieh et al. [60] found that a 16 nm thick ALD-Al_2O_3 coating can completely passivate the holes on Gr and effectively block the ingression of H_2O molecules (Figure 10a). The comparison of Cu surface morphologies before and after etching is shown in Figure 10a, where the largely diminished corrosion area on AlD-Al_2O_3/Gr/Cu obviously confirms the effective corrosion resistance of the ALD-Al_2O_3/Gr coating. The significant anticorrosion enhancement of the ALD-Al_2O_3/Gr coating can also be further quantitatively confirmed by the Tafel analysis (Figure 10a), from which the corrosion rate of the Cu sample is derived to be just 1% of that of bare Cu. We have also healed the defects of CVD Gr coatings grown on Cu by precisely depositing hydrophobic 1H, 1H, 2H, and 2H-perfluorooctanethiol (PFOT) molecules with an unprecedented speed (just with 15 min), and the healed coating exhibited robust long-term corrosion resistance (within the testing period of 60 days) [150]. The optical images of Gr/Cu with and without PFOT after ambient corrosion for 30 and 60 days can also clearly show the anticorrosion efficiency of such a PFOT healing strategy (Figure 10b). We used DFT calculations to reveal many in-depth atomistic bonding mechanisms. Although there is strong interfacial bonding between the Gr coating and Cu substrate at the defect sites, and breaking the C–Cu bonds is energy costing, the PFOT adsorbed on defect sites (edges and inside area) can form very strong S–C bonds and S–Cu bonds, resulting in the high adsorption stability of PFOT (with low E_a, Figure 10a) and then the robust service of the PFOT-healed Gr coating.

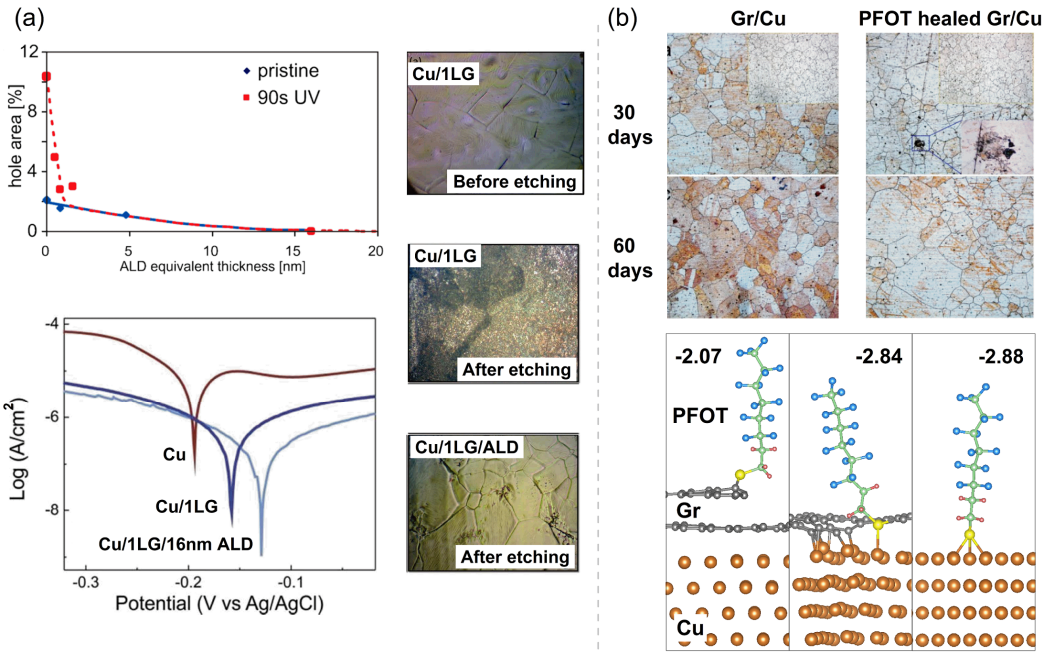

Figure 10. (**a**) Variations in the hole areas with the ALD treatment time for Gr/Cu surfaces with pristine and UV-ozone-treated Gr coatings, optical microscope images of 1LG/Cu before CV corrosion and the etched 1LG/Cu and ALD/1LG/Cu, and Tafel plots of bare Cu, 1LG/Cu, and ALD/1LG/Cu. Adapted with permission from Reference [60]. Copyright 2014, American Chemical Society. (**b**) Optical images of Gr/Cu and PFOT-healed Gr/Cu after the 30-day and 60-day ambient corrosion testings, and the atomic structures for the adsorption of PFOT on Gr patch, vacancy edge, and Cu surface, with the adsorption energies (in eV) of PFOT labeled alongside. Adapted with permission from Reference [150].

5. Conclusions and Future Perspectives

Two-dimensional Gr and h-BN coatings have the intrinsic capability to provide effective protection for various metals, but several problems still largely limit their anticorrosion performance and large-scale applications. An in-depth understanding of the couplings between 2D coatings, metal substrates, and environmental substances is prerequisite for

the precise material designs and property optimizations. Density-functional theory is an accurate and efficient theoretical tool for disentangling the microscopic mechanisms involved in the complex couplings in corrosion processes is powerful in quantitatively assessing the service performance of 2D coatings and can help propose promising methods to optimize the anticorrosion 2D coatings. In this review, we intend to establish the links between microscopic mechanisms revealed by DFT calculations with various experimental syntheses and characterizations, where we try to build a series of unified mechanisms to explain the multiple-factor couplings between coating defects, coating–metal interfaces, and environmental substances involved in the corrosion processes. Based on the established microscopic-mechanism understandings, we both summarize and propose many promising optimization methods (e.g., surface modification, substrate design, interface enhancement, defect healing) to overcome the existing shortcomings of 2D coatings. It can be anticipated that the mechanism understandings and material designs that are systematically discussed here will motivate the further development and research on novel superior anticorrosion 2D coatings working in many multiple-field-coupled environments (e.g., heat, solution, atmosphere, stress, electrostatic field, irradiation), and will become especially indispensable for the design and study of some complex coating architectures consisting of 2D coatings, metal–oxide bond layers, and alloy substrates.

Designing better corrosion-resistant materials, inventing efficient and economic anticorrosion approaches, and in-time intelligent corrosion warning and protection should be the main tasks for experimental and theoretical researchers to pursue in any time. Designing innovative strategies to realize superb corrosion resistance is the driving force for research on 2D coatings. According to the discussion in this review, effectively passivating the defects in 2D coatings and strongly combining 2D coatings with metal–oxide substrates should be two essential directions for researchers to focus on, which can speed up the progress to find out the appropriate 2D coatings and substrate materials, as well as the optimal architectures consisting of them, working under a given environmental condition. This indicates much future work on the exploration of various chemical compositions and structures for the 2D coatings, substrates, and modification agents. The complex couplings between a given coating–substrate architecture and various environmental factors in multiple spatial and temporal scales still need a unified theory system, as well as efficient and accurate first-principles simulation methods.

More state-of-the-art first-principles approaches still need to be developed, which makes it possible to further accurately simulate the dynamic evolution of complex coating systems under the influence of multiple environmental factors. As a young research field, first-principles computational corrosion only has some preliminary development in the previous 10 years [17]. It is the highly interdisciplinary nature that has largely delayed this field, where the metallurgical, physical, and chemical issues may need to be simultaneously solved for one corrosion problem. For example, deeply mastering the theoretical principles in DFT requires talents from the quantum-mechanical world, while developing advanced DFT-based computational methods to efficiently solve many important corrosion problems, as well as reliably proposing promising anticorrosion schemes, requires these DFT researchers being able to fluently combine the relevant metallurgical, physical, and chemical knowledge into one theoretical framework. In addition, the capabilities to read out key information from frequently messy experimental phenomena and have fruitful discussion with corrosion experimentalists are also highly required for the DFT researchers to correctly understand realistic corrosion problems and design appropriate anticorrosion approaches.

Funding: The authors are funded by the Ningbo Natural Science Foundation (Grant No. 2021J229), the Program of Ningbo 3315 Plan (Grant No. 2019A-17-G), the Zhejiang Provincial Natural Science Foundation of China (Grant No. LR21E050001), and the National Natural Science Foundation of China (Grant No. 52105230).

Data Availability Statement: Not applicable.

Acknowledgments: The Supercomputing Center at the Ningbo Institute of Materials Technology is acknowledged for providing the computing resources.

Conflicts of Interest: The authors declare no conflict of interest.

References

1. Hou, B.; Li, X.; Ma, X.; Du, C.; Zhang, D.; Zheng, M.; Xu, W.; Lu, D.; Ma, F. The cost of corrosion in China. *Npj Mater. Degrad.* **2017**, *4*, 1–10.
2. Bunch, J.S.; Verbridge, S.S.; Alden, J.S.; Zande, A.M.; Parpia, J.M.; Craighead, H.G.; McEuen, P.L. Impermeable atomic membranes from graphene sheets. *Nano Lett.* **2008**, *8*, 2458–2462. [CrossRef] [PubMed]
3. Li, L.H.; Ying, C. Atomically thin boron nitride: Unique properties and applications. *Adv. Funct. Mater.* **2016**, *26*, 2594–2608. [CrossRef]
4. Nair, R.R.; Blake, P.; Grigorenko, A.N.; Novoselov, K.S.; Booth, T.J.; Stauber, T.; Peres, N.M.R.; Geim, A.K. Fine Structure Constant Defines Visual Transparency of Graphene. *Science* **2008**, *320*, 1308. [CrossRef]
5. Lee, C.; Wei, X.; Kysar, W.J.; Hone, J. Measurement of the Elastic Properties and Intrinsic Strength of Monolayer Graphene. *Science* **2008**, *321*, 385–388. [CrossRef] [PubMed]
6. Weiss, N.O.; Zhou, H.; Liao, L.; Liu, Y.; Jiang, S.; Huang, Y.; Duan, X. Graphene: An emerging electronic material. *Adv. Mater.* **2012**, *24*, 5782–5825. [CrossRef]
7. Pakdel, A.; Bando, Y.; Golberg, D. Nano boron nitride flatland. *Chem. Soc. Rev.* **2014**, *43*, 934–959. [CrossRef]
8. Lin, L.; Peng, H.; Liu, Z. Synthesis challenges for graphene industry. *Nat. Mater.* **2019**, *18*, 520–529. [CrossRef]
9. Morrow, W.K.; Pearton, S.J.; Ren, F. Review of graphene as a solid state diffusion barrier. *Small* **2016**, *12*, 120–134. [CrossRef] [PubMed]
10. Ding, R.; Li, W.; Wang, X.; Gui, T.; Li, B.; Han, P.; Tian, H.; Liu, A.; Wang, X.; Liu, X.; et al. A brief review of corrosion protective films and coatings based on graphene and graphene oxide. *J. Alloys Compd.* **2018**, *764*, 1039–1055. [CrossRef]
11. Cui, G.; Bi, Z.; Zhang, R.; Liu, J.; Yu, X.; Li, Z. A comprehensive review on graphene-based anti-corrosive coatings. *Chem. Eng. J.* **2019**, *373*, 104–121. [CrossRef]
12. Camilli, L.; Yu, F.; Cassidy, A.; Hornekaer, L.; Boggild, P. Challenges for continuous graphene as a corrosion barrier. *2D Materials* **2019**, *6*, 022002. [CrossRef]
13. Yang, M.; Liu, Y.; Fan, T.; Zhang, D. Metal-graphene interfaces in epitaxial and bulk systems: A review. *Prog. Mater. Sci.* **2020**, *110*, 100652–100708. [CrossRef]
14. Sun, W.; Yang, Y.; Yang, Z.; Wang, L.; Wang, J.; Xu, D.; Liu, G. Review on the corrosion-promotion activity of graphene and its inhibition. *J. Mater. Sci. Technol.* **2021**, *91*, 278–306. [CrossRef]
15. Li, X.; Long, Y.; Ma, L.; Li, J.; Yin, J.; Guo, W. Coating performance of hexagonal boron nitride and graphene layers. *2D Mater.* **2021**, *8*, 034002. [CrossRef]
16. Martin, R.M. *Electronic Structure: Basic Theory and Practical Methods*; Cambridge University Press: Cambridge, UK, 2004.
17. Huang, L.-F.; Scully, J.R.; Rondinelli, J.M. Modeling corrosion with first-principles electrochemical phase diagrams. *Annu. Rev. Mater. Res.* **2019**, *49*, 53–77. [CrossRef]
18. Hafner, J.; Wolverton, C.; Ceder, G. Toward computational materials design: The impact of density functional theory on materials research. *MRS Bull.* **2006**, *31*, 659–668. [CrossRef]
19. Hohenberg, P.; Kohn, W. Inhomogeneous electron gas. *Phys. Rev.* **1964**, *136*, B864–B871. [CrossRef]
20. Kohn, W.; Sham, L.J. Self-consistent equations including exchange and correlation effects. *Phys. Rev.* **1965**, *140*, A1133–A1138. [CrossRef]
21. Ceperley, D.M.; Alder, B.J. Ground state of the electron gas by a stochastic method. *Phys. Rev. Lett.* **1980**, *4*, 566–569. [CrossRef]
22. Perdew, J.P.; Zunger, A. Self-interaction correction to density-functional approximations for many-electron systems. *Phys. Rev. B* **1981**, *23*, 5048–5079. [CrossRef]
23. Perdew, J.P.; Burke, K.; Ernzerhof, M. Generalized gradient approximation made simple. *Phys. Rev. Lett.* **1996**, *77*, 3865–3868. [CrossRef]
24. Perdew, J.P.; Ruzsinszky, A.; Csonka, G.I.; Vydrov, O.A.; Scuseria, G.E.; Constantin, L.A.; Zhou, X.; Burke, K. Restoring the density-gradient expansion for exchange in solids and surfaces. *Phys. Rev. Lett.* **2008**, *100*, 136406. [CrossRef]
25. Tao, J.; Perdew, J.P.; Staroverov, V.N.; Scuseria, G.E. Climbing the density functional ladder: Nonempirical meta-generalized gradient approximation designed for molecules and solids. *Phys. Rev. Lett.* **2003**, *91*, 146401. [CrossRef]
26. Perdew, J.P.; Ruzsinszky, A.; Csonka, G.I.; Constantin, L.A.; Sun, J. Workhorse semilocal density functional for condensed matter physics and quantum chemistry. *Phys. Rev. Lett.* **2009**, *103*, 026403. [CrossRef]
27. Sun, J.; Haunschild, R.; Xiao, B.; Bulik, I.W.; Scuseria, G.E.; Perdew, J.P. Semilocal and hybrid meta-generalized gradient approximations based on the understanding of the kinetic-energy-density dependence. *J. Chem. Phys.* **2013**, *138*, 044113. [CrossRef]
28. Sun, J.; Ruzsinszky, A.; Perdew, J.P. Strongly constrained and appropriately normed semilocal density functional. *Phys. Rev. Lett.* **2015**, *115*, 036402. [CrossRef] [PubMed]
29. Becke, A.D. A new mixing of Hartree-Fock and local density-functional theories. *J. Chem. Phys.* **1993**, *98*, 1372–1377. [CrossRef]

30. Paier, J.; Marsman, M.; Kresse, G. Why does the B3LYP hybrid functional fail for metals? *J. Chem. Phys.* **2007**, *127*, 024103. [CrossRef] [PubMed]
31. Perdew, J.P.; Ernzerhof, M.; Burke, K. Rationale for mixing exact exchange with density functional approximations. *J. Chem. Phys.* **1996**, *105*, 9982–9985. [CrossRef]
32. Heyd, J.; Scuseria, G.E.; Ernzerhof, M. Hybrid functionals based on a screened Coulomb potential. *J. Chem. Phys.* **2003**, *118*, 8207–8215; Erratum in **2006**, *124*, 19906.
33. Vydrov, O.A.; Heyd, J.; Krukau, A.V.; Scuseria, G. E Importance of short-range versus long-range Hartree-Fock exchange for the performance of hybrid density functionals. *J. Chem. Phys.* **2006**, *125*, 074106. [CrossRef]
34. Paier, J.; Marsman, M.; Hummer, K.; Kresse, G.; Gerber, I.C.; A´ngya´n, J.G. Screened hybrid density functionals applied to solids. *J. Chem. Phys.* **2006**, *124*, 154709. [CrossRef]
35. Chen, S.; Brown, L.; Levendorf, M.; Cai, W.; Ju, S.; Edgeworth, J.; Li, X.; Magnuson, C.W.; Velamakanni, A.; Piner, R.D.; et al. Oxidation resistance of graphene-coated Cu and Cu/Ni alloy. *ACS Nano* **2011**, *5*, 1321–1327. [CrossRef]
36. Prasai, D.; Tuberquia, J.C.; Harl, R.R.; Jennings, G.K.; Bolotin, K.I. Graphene: Corrosion-inhibiting coating. *ACS Nano* **2019**, *6*, 1102–1108. [CrossRef]
37. Huang, L.-F.; Santucci, R.J.; Hutchinson, M.; Scully, J.R.; Rondinelli, J.M. Improved electrochemical phase diagrams from theory and experiment: The Ni-water system and its complex compounds. *J. Phys. Chem. C* **2017**, *121*, 9782–9789. [CrossRef]
38. Huang, L.-F.; Rondinelli, J.M. Reliable electrochemical phase diagrams of magnetic transition metals and their complex compounds from ab-initio high-throughput calculations. *Npj Mater. Degrad.* **2019**, *3*, 26. [CrossRef]
39. Zhu, M.; Du, Z.; Yin, Z.; Zhou, W.; Liu, Z.; Tsang, S.H.; Teo, E.H.T. Low-temperature in situ growth of graphene on metallic substrates and its application in anticorrosion. *ACS Appl. Mater. Interfaces* **2016**, *8*, 502–510. [CrossRef] [PubMed]
40. Zhao, Z.; Hou, T.; Wu, N.; Jiao, S.; Zhou, K.; Yin, J.; Suk, J.W.; Cui, X.; Zhang, M.; Li, S.; et al. Polycrystalline few-Layer graphene as a durable anticorrosion film for copper. *Nano Lett.* **2021**, *21*, 1161–1168. [CrossRef]
41. Cui, C.; Lim, A.T.O.; Huang, J. A cautionary note on graphene anticorrosion coatings. *Nat. Nanotechnol.* **2017**, *12*, 834–835. [CrossRef]
42. Cabrera, N.; Mott, N.F. Theory of the oxidation of metals. *Rep. Prog. Phys.* **1949**, *12*, 163. [CrossRef]
43. Atkinson, A. Transport processes during the growth of oxide films at elevated temperature. *Rev. Mod. Phys.* **1985**, *57*, 437. [CrossRef]
44. Baran, J.D.; Grönbeck, H.; Hellman, A. Mechanism for Limiting Thickness of Thin Oxide Films on Aluminum. *Phys. Rev. Lett.* **2014**, *112*, 146103. [CrossRef] [PubMed]
45. Li, L.H.; Xing, T.; Chen, Y.; Jones, R. Boron nitride nanosheets for metal protection. *Adv. Mater. Interfaces* **2014**, *1*, 1300132–1300138. [CrossRef]
46. Zhang, J.; Yang, Y.; Lou, J. Investigation of hexagonal boron nitride as an atomically thin corrosion passivation coating in aqueous solution. *Nanotechnology* **2016**, *27*, 364004–364010. [CrossRef]
47. Shen, L.; Zhao, Y.; Wang, Y.; Song, R.; Yao, Q.; Chen, S.; Chai, Y. A long-term corrosion barrier with an insulating boron nitride monolayer. *J. Mater. Chem. A* **2016**, *4*, 5044–5050. [CrossRef]
48. Chilkoor, G.; Jawaharraj, K.; Vemuri, B.; Kutana, A.; Tripathi, M.; Kota, D.; Arif, T.; Filleter, T.; Dalton, A.B.; Yakobson, B.I.; et al. Hexagonal boron nitride for sulfur corrosion inhibition. *ACS Nano* **2020**, *14*, 14809–14819. [CrossRef] [PubMed]
49. Chilkoor, G.; Karanam, S.P.; Star, S.; Sani, R.K.; Upadhyayula, V.K.K.; Ghoshal, D.; Koratkar, A.N.; Meyyappan, M.; Gadhamshetty, V. Hexagonal boron nitride: The thinnest insulating barrier to microbial corrosion. *ACS Nano* **2018**, *12*, 2242–2252. [CrossRef]
50. Ye, C.; Zhu, Y.; Sun, H.; Chen, F.; Sun, H.; Dai, W.; Wei, Q.; Li, F.; Yu, A.; Du, S.; et al. Layer-by-layer stacked graphene nanocoatings by Marangoni self-assembly for corrosion protection of stainless steel. *Chin. Chem. Lett.* **2021**, *32*, 501–505. [CrossRef]
51. Scardamaglia, M.; Boix, V.; D'Acunto, G.; Struzzi, C.; Reckinger, N.; Chen, X.; Shivayogimath, A.; Booth, T.; Knudsen, C. Comparative study of copper oxidation protection with graphene and hexagonal boron nitride. *Carbon* **2021**, *171*, 610–617. [CrossRef]
52. Galbiati, M.; Stoot, A.C.; Mackenzie, D.M.A.; Bøgild, P.; Camilli, L. Real-time oxide evolution of copper protected by graphene and boron nitride barriers. *Sci. Rep.* **2017**, *7*, 39770.
53. Li, P.; Ju, P.; Ji, L.; Li, H.; Liu, X.; Chen, L.; Zhou, H.; Chen, J. Toward Robust Macroscale Superlubricity on Engineering Steel Substrate. *Adv. Mater.* **2020**, *32*, 2002039. [CrossRef] [PubMed]
54. Egberts, P.; Han, G.H.; Liu, X.Z.; Johnson, A.T.C.; Carpick, R.W. Frictional behavior of atomically grown on copper by chemical vapor deposition. *ACS Nano* **2014**, *8*, 5010–5021. [CrossRef] [PubMed]
55. Li, Q.; Lee, C.; Carpich, R.W.; Hone, J. Substrate effect on thickness-dependent friction on graphene. *Phys. Status Solidi (b)* **2010**, *247*, 2909–2914. [CrossRef]
56. Qu, C.; Wang, K.; Wang, J.; Gongyang, Y.; Carpick, R.W.; Urbakh, M.; Zheng, Q. Origin of friction in superlubric graphite contacts. *Phys. Rev. Lett.* **2020**, *125*, 126102. [CrossRef] [PubMed]
57. Qi, Y.; Liu, J.; Dong, Y.; Feng, X.-Q.; Li, Q. Impacts of environments on nanoscale wear behavior of graphene: Edge passivation vs. substrate pinning. *Carbon* **2018**, *139*, 59–66. [CrossRef]
58. Rowe, G.W. Some observations on the frictional behaviour of boron nitride and of graphite. *Wear* **1960**, *3*, 274–285. [CrossRef]
59. Zhao, X.; Zhang, G.; Wang, L.; Xue, Q. The Tribological Mechanism of MoS_2 Film under Different Humidity. *Tribol. Lett.* **2017**, *65*, 64. [CrossRef]

60. Hsieh, Y.-P.; Hofmann, M.; Chang, K.-W.; Jhu, J.G.; Li, Y.-Y.; Chen, K.Y.; Yang, C.C.; Chang, W.-S.; Chen, L.-C. Complete corrosion inhibition through graphene defect passivation. *ACS Nano* **2014**, *8*, 443–448. [CrossRef]
61. Christian, M.S.; Johnson, E.R. Effect of a metal substrate on interlayer interactions in bilayer graphene. *J. Phys. Chem. C* **2018**, *122*, 8910–8918. [CrossRef]
62. Weatherup, R.S.; D'Arsié, L.; Cabrero-Vilatela, A.; Caneva, S.; Blume, R.; Robertson, J.; Schlögl, R.; Hofmann, S. Long–term passivation of strongly interacting metals with single-layer graphene. *J. Am. Chem. Soc.* **2015**, *137*, 14358–14366. [CrossRef]
63. Kyhl, L.; Balog, R.; Cassidy, A.; Jørgensen, J.; Grubisic-Cabo, A.; Trotochaud, L.; Bluhm, H.; Hornekær, L. Enhancing graphene protective coatings by hydrogen-induced chemical bond formation. *ACS Appl. Nano Mater.* **2018**, *1*, 4509–4515. [CrossRef]
64. Xu, X.; Yi, D.; Wang, Z.; Yu, J.; Zhang, Z.; Qiao, R.; Sun, Z.; Hu, Z.; Gao, P.; Peng, H.; et al. Greatly enhanced anticorrosion of Cu by commensurate graphene coating. *Adv. Mater.* **2017**, *30*, 1702944. [CrossRef]
65. Luo, B.; Koleini, M.; Whelan, P.R.; Shivayogimath, A.; Brandbyge, M.; Boggild, P. Booth, T.J. Graphene-subgrain-defined oxidation of copper. *ACS Appl. Mater. Interfaces* **2019**, *11*, 48518–48524. [CrossRef] [PubMed]
66. Braeuninger-Weimer, P.; Burton, O.J.; Zeller, P.; Amati, M.; Gregoratti, L.; Weatherup, R.S.; Hofmann, S. Crystal orientation dependent oxidation modes at the buried graphene-Cu interface. *Chem. Mater.* **2020**, *32*, 7766–7776. [CrossRef] [PubMed]
67. Luo, D.; Wang, X.; Li, B.-W.; Zhu, C.; Huang, M.; Qiu, L.; Wang, M.; Jin, S.; Kim, M.; Ding, F.; et al. The wet-oxidation of a Cu(111) foil coated by single crystal graphene. *Adv. Mater.* **2021**, *33*, 2102697. [CrossRef]
68. Ye, Z.; Balkanci, A.; Martini, A.; Baykara, M.Z. Effect of roughness on the layer-dependent friction of few-layer graphene. *Phys. Rev. B* **2017**, *96*, 115401. [CrossRef]
69. Tripathi, M.; Awaja, F.; Paolicelli, G.; Bartali, R.; Iacob, E.; Valeri, S.; Ryu, S.; Signetti, S.; Speranza, G.; Pugno, N.M. Tribological characteristics of few-layer graphene over Ni grain and interface boundaries. *Nanoscale* **2016**, *8*, 6646–6658. [CrossRef]
70. Klemenz, A.; Pastewka, L.; Balakrishna, S.G.; Caron, A.; Bennewitz, R.; Moseler, M. Atomic Scale Mechanisms of Friction Reduction and Wear Protection by Graphene. *Nano Lett.* **2014**, *14*, 7145–7152. [CrossRef]
71. Tripathi, M.; Awaja, F.; Bizao, R.A.; Signetti, S.; Iacob, E.; Paolicelli, G.; Valeri, S.; Dalton, A.; Pugno, N.M. Friction and Adhesion of Different Structural Defects of Graphene. *ACS Appl. Mater. Interfaces* **2018**, *10*, 44614–44623. [CrossRef] [PubMed]
72. Long, F.; Yasaei, P.; Yao, W.; Salehi-Khojin, A.; Shahbazian-Yassar, R. Anisotropic Friction of Wrinkled Graphene Grown by Chemical Vapor Deposition. *ACS Appl. Mater. Interfaces* **2017**, *9*, 20922–20927. [CrossRef]
73. Yang, K.M.; Tang, P.Z.; Zhang, Q.; Ma, H.Y.; Liu, E.Q.; Li, M.; Zhang, X.; Li, J.; Liu, Y.; Fan, T.X. Enhanced defect annihilation capability of the graphene/copper interface: An in situ study. *Scr. Mater.* **2021**, *203*, 114001. [CrossRef]
74. Kim, Y.; Baek, J.; Kim, S.; Kim, S.; Ryu, S.; Jeon, S.; Han, S.M. Radiation resistant vanadium-graphene nanolayered composite. *Sci. Rep.* **2016**, *6*, 24785. [CrossRef]
75. Si, S.; Li, W.; Zhao, X.; Han, M.; Yue, Y.; Wu, W.; Guo, S.; Zhang, X.; Dai, Z.; Wang, X.; et al. Significant radiation tolerance and moderate reduction in thermal transport of a tungsten nanofilm by inserting monolayer graphene. *Adv. Mater.* **2017**, *29*, 1604623. [CrossRef] [PubMed]
76. Berry, V. Impermeability of graphene and its applications. *Carbon* **2013**, *62*, 1–10. [CrossRef]
77. Zhao, Y.; Xie, Y.; Liu, Z.; Wang, X.; Chai, Y.; Yan, F. Two-dimensional material membranes: An emerging platform for controllable mass transport applications. *Small* **2014**, *10*, 4521–4542. [CrossRef]
78. Liu, K.; Zhang, G.; Pu, J.; Ma, F.; Wu, G.; Lu, Z. Impermeability of boron nitride defect-sensitive monolayer with atomic-oxygen-healing ability. *Ceram. Int.* **2018**, *44*, 13888–13893. [CrossRef]
79. Schriver, M.; Regan, W.; Gannett, W.J.; Zaniewski, A.M.; Crommie, M.F.; Zettl, A. Graphene as a long-term metal oxidation barrier: Worse than nothing. *ACS Nano* **2013**, *7*, 5763–5768. [CrossRef]
80. Dong, Y.; Liu, Q.; Zhou, Q. Corrosion behavior of Cu during graphene growth by CVD. *Corros. Sci.* **2014**, *89*, 214–219. [CrossRef]
81. Zhang, Y.H.; Wang, B.; Zhang, H.R.; Chen, Z.Y.; Zhang, Y.Q.; Wang, B.; Sui, Y.P.; Li, X.L.; Xie, X.M.; Yu, G.H.; et al. The distribution of wrinkles and their effects on the oxidation resistance of chemical vapor deposition graphene. *Carbon* **2014**, *70*, 81–86. [CrossRef]
82. Zhang, Y.H.; Zhang, H.R.; Wang, B.; Chen, Z.Y.; Zhang, Y.Q.; Wang, B.; Sui, Y.P.; Zhu, B.; Tang, C.M.; Li, X.L.; et al. Role of wrinkles in the corrosion of graphene domain-coated Cu surfaces. *Appl. Phys. Lett.* **2014**, *104*, 143110–143113. [CrossRef]
83. Kidambi, P.R.; Bayer, B.C.; Blume, R.; Wang, Z.-J.; Baehtz, C.; Weatherup, R.S.; Willinger, M.-G.; Schloegl, R.; Hofmann, S. Observing graphene grow: Catalyst–graphene interactions during scalable graphene growth on polycrystalline copper. *Nano Lett.* **2013**, *13*, 4769–4778. [CrossRef]
84. Dlubak, B.; Martin, M.-B.; Weatherup, R.S.; Yang, H.; Deranlot, C.; Blume, R.; Schloegl, R.; Fert, A.; Anane, A.; Hofmann, S.; et al. Graphene–passivated nickel as an oxidation-resistant electrode for spintronics. *ACS Nano* **2012**, *6*, 10930–10934. [CrossRef]
85. Martin, M.-B.; Dlubak, B.; Weatherup, R.S.; Yang, H.; Deranlot, C.; Bouzehouane, K.; Petroff, F.; Anane, A.; Hofmann, S.; Robertson, J.; et al. Sub–nanometer atomic layer deposition for spintronics in magnetic tunnel junctions based on graphene spin-filtering membranes. *ACS Nano* **2014**, *8*, 7890–7895. [CrossRef] [PubMed]
86. Grånäs, E.; Knudsen, J.; Schroder, U.A.; Gerber, T.; Busse, C.; Arman, M.A.; Schulte, K.; Andersen, J.N.; Michely, T. Oxygen intercalation under graphene on Ir(111): Energetics, kinetics, and the role of graphene edges. *ACS Nano* **2012**, *11*, 9951–9963. [CrossRef]
87. Dong, Y.; Liu, Q.; Zhou, Q. Time-dependent protection of ground and polished Cu using graphene film. *Corros. Sci.* **2015**, *90*, 69–75. [CrossRef]

88. Anisur, M.R.; Banerjee, P.C.; Easton, C.D. Controlling hydrogen environment and cooling during CVD graphene growth on nickel for improved corrosion resistance. *Carbon* **2018**, *127*, 131–140. [CrossRef]
89. Surwade, S.P.; Li, Z.; Liu, H. Thermal oxidation and unwrinkling of chemical vapor deposition-grown graphene. *J. Phys. Chem. C* **2012**, *116*, 20600–20606. [CrossRef]
90. Ren, S.; Hao, Y.; Cui, M.; Pu, J.; Huang, L.-F.; Wang, L. Correlated morphological and chemical mechanisms for the superior corrosion resistance of alumina-deposited 2D nanofilms on copper. *Materialia* **2020**, *11*, 100697–100708. [CrossRef]
91. Zhang, H.; Ren, S.; Pu, J.; Xue, Q. Barrier mechanism of multilayers graphene coated copper against atomic oxygen irradiation. *Appl. Surf. Sci.* **2018**, *444*, 28–35. [CrossRef]
92. Tiwari, A.; Raman, R.K.S. Durable corrosion resistance of copper due to multi-layer graphene. *Materials* **2017**, *10*, 1112. [CrossRef]
93. Sun, T.-Y.; Hao, Y.; Lin, C.-T.; Wang, L.; Huang, L.-F. Unraveling the strong coupling between graphene/nickel interface and atmospheric adsorbates for versatile realistic applications. *Carbon Trends* **2021**, *2*, 100013–100024. [CrossRef]
94. Kim, H.G.; Lee, H.-B.-R. Atomic layer deposition on 2D materials. *Chem. Mater.* **2017**, *29*, 3809–3826. [CrossRef]
95. Chang, M.L.; Cheng, T.C.; Lin, M.C.; Lin, H.C.; Chen, M.J. Improvement of oxidation resistance of copper by atomic layer deposition. *Appl. Surf. Sci.* **2012**, *258*, 10128–10134. [CrossRef]
96. Bahari, H.S.; Savaloni, H. Surface analysis of Cu coated with ALD Al_2O_3 and its corrosion protection enhancement in NaCl solution: EIS and polarization. *Mater. Res. Express* **2019**, *6*, 086570–086615. [CrossRef]
97. Dahal, A.; Batzill, M. Graphene–nickel interfaces: A review. *Nanoscale* **2014**, *6*, 2548–2562. [CrossRef]
98. Mittendorfer, F.; Garhofer, A.; Redinger, J.; Klimeš, J.; Harl, J.; Kresse, G. Graphene on Ni(111): Strong interaction and weak adsorption. *Phys. Rev. B* **2011**, *84*, 201401. [CrossRef]
99. Khomyakov, P.A.; Giovannetti, G.; Rusu, P.C.; Brocks, G.; van den Brink, J.; Kelly, P.J. First-principles study of the interaction and charge transfer between graphene and metals. *Phys. Rev. B* **2009**, *79*, 195425. [CrossRef]
100. Giovannetti, G.; Khomyakov, P.A.; Brocks, G.; Karpan, V.M.; van den Brink, J.; Kelly, P.J. Doping Graphene with Metal Contacts. *Phys. Rev. Lett.* **2009**, *101*, 026803–026806. [CrossRef]
101. Olsen, T.; Yan, J.; Mortensen, J.J.; Thygesen, K.S. Dispersive and covalent interactions between graphene and metal surfaces from the random phase approximation. *Phys. Rev. Lett.* **2011**, *107*, 156401. [CrossRef] [PubMed]
102. Andersen, M.; Hornekær, L.; Hammer, B. Graphene on metal surfaces and its hydrogen adsorption: A meta-GGA functional study. *Phys. Rev. B* **2012**, *86*, 18559. [CrossRef]
103. Kozlov, S.; Viñes, F.; Görling, A. Bonding mechanisms of graphene on metal surfaces. *J. Phys. Chem. C* **2012**, *116*, 7360–7366. [CrossRef]
104. Sun, J.; Xiao, B.; Fang, Y.; Haunschild, R.; Hao, P.; Ruzsinszky, A.; Csonka, G.; Scuseria, G.; Perdew, J. Density functionals that recognize covalent, metallic, and weak bonds. *Phys. Rev. Lett.* **2013**, *111*, 106401. [CrossRef]
105. Auwärter, W. Hexagonal boron nitride monolayers on metal supports: Versatile templates for atoms, molecules and nanostructures. *Surf. Sci. Rep.* **2019**, *74*, 1–95. [CrossRef]
106. Koitz, R.; Nørskov, J.K.; Studt, F. A systematic study of metal-supported boron nitride materials for the oxygen reduction reaction. *Phys. Chem. Chem. Phys.* **2015**, *17*, 12722–12727. [CrossRef]
107. Joshi, N.; Ghosh, P. Substrate-induced changes in the magnetic and electronic properties of hexagonal boron nitride. *Phys. Rev. B* **2013**, *87*, 235440. [CrossRef]
108. Muntwiler, M.; Zhang, J.; Stania, R.; Matsui, F.; Oberta, P.; Flechsig, U.; Patthey, L.; Quitmann, C.; Glatzel, T.; Widmer, R.; et al. Surface science at the PEARL beamline of the swiss light source. *J. Synchrotron Radiat.* **2017**, *24*, 354–366. [CrossRef] [PubMed]
109. Brülke, C.; Heepenstrick, T.; Humberg, N.; Krieger, I.; Sokolowski, M.; Weıı, S.; Tautz, T.S.; Soubatch, S. Long vertical distance bonding of the hexagonal boron nitride monolayer on the Cu(111) surface. *J. Phys. Chem. C* **2017**, *121*, 23964–23973. [CrossRef]
110. Schwarz, M.; Riss, A.; Garnica, M.; Ducke, J.; Deimel, P.S.; Duncan, D.A.; Thakur, P.K.; Lee, T.L.; Seitsonen, A.P.; Barth, J.V.; et al. Corrugation in the weakly interacting hexagonal-BN/Cu(111) system: Structure determination by combining noncontact atomic force microscopy and X-ray standing waves. *ACS Nano* **2017**, *11*, 9151–9161. [CrossRef] [PubMed]
111. Kutana, A.; Goriachko, A.; Hu, Z.L.; Sachdev, H.; Over, H.; Yakobson, B.I. Buckling patterns of graphene-boron nitride alloy on Ru(0001). *Appl. Mater. Interfaces* **2015**, *2*, 1500322. [CrossRef]
112. Zhang, Q.; Chen, Y.X.; Zhang, C.D.; Pan, C.R.; Chou, M.Y.; Zeng, C.G.; Shih, C.K. Bandgap renormalization and work function tuning in MoSe2/hBN/Ru(0001) heterostructures. *Nat. Commun.* **2016**, *7*, 13843. [CrossRef]
113. Iannuzzi, M.; Tran, F.; Widmer, R.; Dienel, T.; Radican, K.; Ding, Y.; Hutter, J.R.; Gröning, O. Site-selective adsorption of phthalocyanine on h-BN/Rh(111) nanomesh. *Phys. Chem. Chem. Phys.* **2014**, *16*, 12374–12384. [CrossRef] [PubMed]
114. Ding, Y.; Iannuzzi, M.; Hutter, J. Investigation of boron nitride nanomesh interacting with water. *J. Phys. Chem. C* **2011**, *115*, 13685–13692. [CrossRef]
115. Laskowski, R.; Blaha, P.; Schwarz, K. Bonding of hexagonal BN to transition metal surfaces: An ab initio density-functional theory study. *Phys. Rev. B* **2008**, *78*, 045409. [CrossRef]
116. Bokdam, M.; Brocks, G.; Katsnelson, M.I.; Kelly, P.J. Schottky barriers at hexagonal boron nitride/metal interfaces: A first-principles study. *Phys. Rev. B* **2014**, *90*, 085415. [CrossRef]
117. Qi, Y.; Han, N.N.; Li, Y.C.; Zhang, Z.P.; Zhou, X.B.; Deng, B.; Li, Q.C.; Liu, M.X.; Zhao, J.J.; Liu, Z.F.; et al. Strong adlayer-substrate interactions "break" the patching growth of h-BN onto graphene on Re(0001). *ACS Nano* **2017**, *11*, 1807–1815. [CrossRef] [PubMed]

118. Larciprete, R.; Ulstrup, S.; Lacovig, P.; Dalmiglio, M.; Bianchi, M.; Mazzola, F.; Hornekær, L.; Orlando, F.; Baraldi, A.; Hofmann, P.; et al. Oxygen switching of the epitaxial graphene-metal interaction. *ACS Nano* **2012**, *6*, 9551–9558. [CrossRef]
119. Hagen, F.H.F.; Zimmermann, D.M.; Silva, C.C.; Schlueter, C.; Atodiresei, N.; Jolie, W.; Martínez-Galera, A.J.; Dombrowski, D.; Schröder, U.A.; Will, M.; et al. Structure and growth of hexagonal boron nitride on Ir(111). *ACS Nano* **2016**, *10*, 11012–11026. [CrossRef]
120. Schultz, B.J.; Dennis, R.V.; Lee, V.; Banerjee, S. An electronic structure perspective of graphene interfaces. *Nanoscale* **2014**, *6*, 3444–3466. [CrossRef] [PubMed]
121. Dorward, R.C. Discussion of "Comments on the Solubility of Carbon in Molten Aluminum". *Metall. Trans. A* **1990**, *21*, 255–257. [CrossRef]
122. Sung, C.-M.; Tai, M.-F. Reactivities of transition metals with carbon: Implications to the mechanism of diamond synthesis under high pressure. *Int. J. Refract. Met. Hard Mater.* **1997**, *15*, 237–256. [CrossRef]
123. Sutter, P.; Ciobanu, C.V.; Sutter, E. Real-time microscopy of graphene growth on epitaxial metal films: Role of template thickness and strain. *Small* **2012**, *68*, 2250–2257. [CrossRef]
124. Yoshii, S.; Nazawa, K.; Toyota, K.; Matsukawa, N.; Odagawa, A.; Tsujimura, A. Suppression of inhomogeneous segregation in graphene growth on epitaxial metal films. *Nano Lett.* **2011**, *11*, 2628–2633. [CrossRef]
125. Sutter, P.W.; Flege, J.I.; Sutter, E.A. Epitaxial graphene on ruthenium. *Nat. Mater.* **2008**, *7*, 406–411. [CrossRef]
126. Busse, C.; Lazic, P.; Djemour, R.; Coraux, J.; Gerber, T.; Atodiresei, N. Graphene on Ir(111): Physisorption with Chemical Modulation. *Phys. Rev. Lett.* **2011**, *107*, 036101. [CrossRef] [PubMed]
127. Fukaya, Y.; Entani, S.; Sakai, S.; Mochizuki, I.; Wada, K.; Hyodo, T. Spacing between graphene and metal substrates studied with total-reflection high-energy positron diffraction. *Carbon* **2016**, *103*, 1–4. [CrossRef]
128. Zhao, W.; Kozlov, S.M.; Höfert, O.; Gotterbarm, K.; Lorenz, M.P.A.; Viñes, F.; Papp, C.; Görling, A.; Steinrück, H.-P. Graphene on Ni(111): Coexistence of different surface structures. *J. Phys. Chem. Lett.* **2011**, *2*, 759–764. [CrossRef]
129. Matysik, S.C.; Papp, C.; Goerling, A. Solving the puzzle of the coexistence of different adsorption geometries of graphene on Ni(111). *J. Phys. Chem. Lett.* **2018**, *122*, 26105–26110. [CrossRef]
130. Batzill, M. The surface science of graphene: Metal interfaces, CVD synthesis, nanoribbons, chemical modifications, and defects. *Surf. Sci. Rep.* **2012**, *67*, 83–115. [CrossRef]
131. Müller, F.; Hüfnerb, S.; Sachdev, H. One-dimensional structure of boron nitride on chromium (110)—A study of the growth of boron nitride by chemical vapour deposition of borazine. *Surf. Sci.* **2008**, *602*, 3467–3476. [CrossRef]
132. Kiraly, B.; Jacobberger, R.M.; Mannix, A.J.; Campbell, G.P.; Bedzyk, M.J.; Arnold, M.S. Electronic and Mechanical Properties of Graphene-Germanium Interfaces Grown by Chemical Vapor Deposition. *Nano Lett.* **2015**, *15*, 7414–7420. [CrossRef] [PubMed]
133. Varykhalov, A.; Rader, O. Graphene grown on Co(0001) films and islands: Electronic structure and its precise magnetization dependence. *Phys. Rev. Lett.* **2009**, *80*, 035437. [CrossRef]
134. Sutter, P.; Sadowski, J.T.; Sutter, E. Electronic Structure of Few-Layer Epitaxial Graphene on Ru(0001). *Nano Lett.* **2009**, *9*, 2654–2660. [CrossRef] [PubMed]
135. Kim, G.; Jung, S.C.; Han, Y.-K. Selectively strong molecular adsorption on boron nitride monolayer induced by transition metal substrate. *Curr. Appl. Phys.* **2013**, *13*, 2059–2063. [CrossRef]
136. Kong, L.; Enders, A.; Rahman, T.S.; Dowben, P.A. Molecular adsorption on graphene. *J. Phys. Condens. Matter* **2014**, *26*, 443001. [CrossRef]
137. Rosei, R.; Crescenzi, M.D.; Sette, F.; Quaresima, C.; Savoia, A.; Perfetti, P. Structure of graphitic carbon on Ni(111): A surface extended-energy-loss fine-structure study. *Phys. Rev. B* **1983**, *28*, 1161. [CrossRef]
138. Gamo, Y.; Nagashima, A.; Wakabayashi, M.; Terai, M.; Oshima, C. Atomic structure of monolayer graphite formed on Ni(111). *Surf. Sci.* **1997**, *374*, 61–64. [CrossRef]
139. Huang, L.F.; Ni, M.Y.; Zhneg, X.H.; Zhou, W.H.; Li, Y.G.; Zeng, Z. Ab initio simulation of the kinetic properties of the hydrogen monomer on graphene. *J. Phys. Chem. C* **2010**, *114*, 22636–22643. [CrossRef]
140. Zhu, L.; Zhang, W.; Zhu, J.; Cheng, D. Ni (111)-supported graphene as a potential catalyst for high-efficient CO oxidation. *Carbon* **2017**, *116*, 201–209. [CrossRef]
141. Lyalin, A.; Nakayama, A.; Uosaki, K.; Taketsugu, T. Functionalization of monolayer h-BN by a metal support for the oxygen reduction reaction. *J. Phys. Chem. C* **2013**, *117*, 21359–21370. [CrossRef]
142. Guo, Y.; Guo, W. Hydroxylation of a metal-supported hexagonal boron nitride monolayer by oxygen induced water dissociation. *Phys. Chem. Chem. Phys.* **2015**, *17*, 16428–16433. [CrossRef]
143. Ferrighi, L.; Perilli, D.; Selli, D.; Valentin, C.D. Water at the interface between defective graphene and Cu or Pt (111) surfaces. *ACS Appl. Mater. Interfaces* **2017**, *9*, 29932–29941. [CrossRef]
144. Ambrosetti, A.; Silvestrelli, P.L. Toward tunable CO adsorption on defected graphene: The chemical role of Ni(111) and Cu(111) substrates. *J. Phys. Chem. C* **2017**, *121*, 19828–19835. [CrossRef]
145. Krasheninnikov, A.V.; Berseneva, N.; Kvashnin, D.G.; Enkovaara, J.; Björkmanr, T.; Sorokin, P.; Shtansky, D.; Nieminen, R.M.; Golberg, D. Toward stronger Al-BN nanotube composite materials: Insights into bonding at the Al/BN interface from first-principles calculations. *J. Phys. Chem. C* **2014**, *118*, 26594–26901. [CrossRef]
146. Zhang, X.; Wang, S. Interfacial strengthening of graphene/aluminum composites through point defects: A first-principles study. *Nanomaterials* **2021**, *11*, 738. [CrossRef] [PubMed]

147. Usachov, D.; Adamchuk, V.K.; Haberer, D.; Grüneis, A.; Sachdev, H.; Preobrajenski, A.B.; Laubschat, C.; Vyalikh, D.V. Quasifree-standing single-layer hexagonal boron nitride as a substrate for graphene synthesis. *Phys. Rev. B* **2010**, *82*, 075415. [CrossRef]
148. Jo, M.; Lee, H.C.; Lee, S.G.; Cho, K. Graphene as a metal passivation layer: Corrosion-accelerator and inhibitor. *Carbon* **2017**, *116*, 232–239. [CrossRef]
149. Shang, W.; Wu, F.; Wang, Y.; Baboukani, A.R.; We, Y.; Jiang, J. Corrosion resistance of micro-arc oxidation/graphene oxide composite coatings on magnesium alloys. *ACS Omega* **2020**, *5*, 7262–7270. [CrossRef]
150. Wu, Y.; Sun, T.-Y.; Ge, T.; Zhao, W.; Huang, L.-F. Eliminating the galvanic corrosion effect of graphene coating by an accurate and rapid self-assembling defect healing approach. *Adv. Funct. Mater.* **2021**, in press.